CASL-U-2014-0169-000

Power uprates
and plant life extension

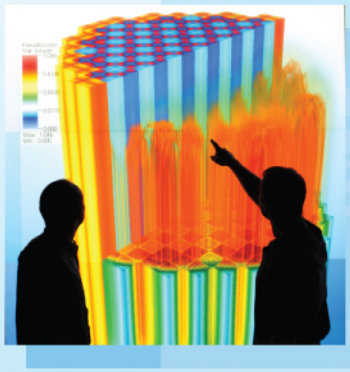

Engineering design
and analysis

Science-enabling
high performance
computing

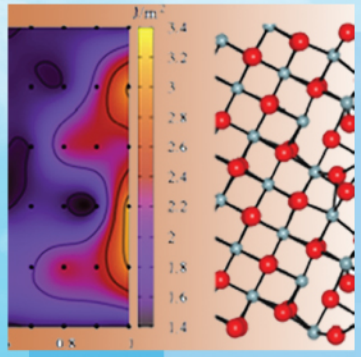

Fundamental science

Plant operational data

CASL-U-2014-0169-000

Consortium for Advanced Simulation of LWRs

L3:PHI.VCS.P9.02
CTF Validation

Robert K. Salko
Oak Ridge National Laboratory

Taylor Blyth, Chris Dances, Jeffrey Mageganz, Maria Avramova
Pennsylvania State University

August 20, 2014

U.S. DEPARTMENT OF ENERGY | Nuclear Energy

The Pennsylvania State University

Department of Mechanical and Nuclear Engineering

Reactor Dynamics and Fuel Management Group

CTF Validation

August 20, 2014

CASL-U-2014-0169-000

Authors:

Robert K. Salko[1]

Taylor S. Blyth[2]

Chris A. Dances[3]

Jeffrey W. Magedanz[4]

Maria N. Avramova[5]

[1] *Oak Ridge National Laboratory* **T:** (856) 576-5339 **E:** salkork@ornl.gov
[2] *Pennsylvania State University* **E:** tyb5095@psu.edu
[3] *Pennsylvania State University* **E:** chris.a.dances@gmail.com
[4] *Pennsylvania State University* **E:** jeff.magedanz@gmail.com
[5] *Pennsylvania State University* **T:** (814) 865-0043 **E:** mna109@psu.edu

Abstract

Coolant-Boiling in Rod Arrays- Two Fluids (COBRA-TF) is a Thermal/Hydraulic (T/H) simulation code designed for Light Water Reactor (LWR) vessel analysis. It uses a two-fluid, three-field (i.e. fluid film, fluid drops, and vapor) modeling approach. Both sub-channel and 3D Cartesian forms of nine conservation equations are available for LWR modeling. The code was originally developed by Pacific Northwest Laboratory in 1980 and has been used and modified by several institutions over the last several decades. COBRA-TF also found use at the Pennsylvania State University (PSU) by the Reactor Dynamics and Fuel Management Group (RDFMG) and has been improved, updated, and subsequently become the PSU RDFMG version of COBRA-TF (CTF). As part of the improvement process, it was necessary to generate sufficient documentation for the open-source code which had lacked such material upon being adopted by RDFMG.

This document seeks to provide a certain level of certainty and confidence in the predictive capabilities of the code for the scenarios it was designed to model—rod bundle geometries with operating conditions that are representative of prototypical Pressurized Water Reactor (PWR)s and Boiling Water Reactor (BWR)s in both normal and accident conditions. This is done by modeling a variety of experiments that simulate these scenarios and then presenting a qualitative and quantitative analysis of the results that demonstrates the accuracy to which CTF is capable of capturing specific quantities of interest.

CONTENTS

LIST OF FIGURES

CHAPTER 1

INTRODUCTION

The process of modeling and simulating a physical system or phenomena is a complex process involving several steps. We must formulate a mathematical model that suitably describes the physics we look to model, we need to then come up with a way to solve that mathematical model, and finally, we need to then translate all these steps into machine language in the form of a computer program so as to make the method useful for solving real problems. There is a lot that can go wrong in this process. Code testing is what we use to mitigate the potential for such problems. A code that is devoid of proper and sufficient testing is one of limited use, as we cannot know that the code is capable of performing its advertised capabilities.

Being that the process of developing the tools used for doing the modeling and simulation is a complex process, it is no surprise that testing them is also a complex, multi-stage process. Properly testing a code can be divided into six steps:

1. Formulate code requirements
2. Document the code theory
3. Employ and document code Quality Assurance (QA) procedures
4. Perform and document verification studies
5. Perform and document validation studies
6. Perform and document uncertainty quantification studies

The first step involves stating what it is that the code can and cannot do. The user needs to know this first to know how to properly use the tool. Every step after this is geared towards backing up the claims that are made in this document. The requirements, or features, of CTF are summarized in Chapter 2.

The second step instructs the user how the code features are implemented in the code. In other words, it documents the mathematical models that are employed to model the physics the code intends to capture. In addition to that, it also says how the governing equations are closed (constitutive models), and how they are solved (numerical methods). The CTF Theory Manual[9] is provided directly in the COBRA-TF repository in the "doc" directory alongside this manual.

The models that were discussed in the theory manual do little good as equations on paper—they need to be coded up into a machine language that is eventually compiled and used to run simulations. This "coding up" phase invites many opportunities to make mistakes, introducing defects into the code models. The QA process is meant to prevent these "bugs" from getting into the code and assuring that the models are working as intended. Currently, there is a QA process in place for CTF, but there is limited documentation on this procedure. Briefly, the Git version control system is utilized to track all changes made to the source code. Next, selected individual models are unit tested to ensure proper functioning at the finest unit of granularity. At the next level, we perform regression tests that cover a multitude of geometries and operating conditions meant to activate the most important features and capabilities of CTF. Both of these types of tests are run automatically on a regular basis and the results are checked against "gold" results that are deemed correct. This both ensures proper functionality and prevents loss of functionality during normal development activities. Finally, Valgrind testing is performed on the regression suite to alert us to memory-related defects in the code.

The fourth step involves demonstrating that the mathematical models behave as expected and, as a second step, presents the numerical error of the models chosen. There is currently limited verification work done on CTF.

The fifth step involves measuring the performance of the physical models in the code, demonstrating that they are implemented correctly, and assessing their accuracy at predicting real world physics. A necessary part of this step is to compare code results against actual experimental data. This step is meant to be covered by this document.

The final stage of code testing is putting error bars on the results that the code produces. These error bars tell us how certain we can be in the results we get. They are a combination of the uncertainty in the input data given to the code, the uncertainty in the physical models we have employed, and the numerical error in our mathematical modeling approach. This process has yet to be completed for CTF.

The outlined process is one that should be undertaken simultaneously with code development, as the cost of finding code bugs increases at an exponential rate with respect to time left in the code. Ideally, to encourage regular code testing, and to improve user confidence, the full process should be automated. The QA regression suite, verification suite, and validation suite of tests should be able to be run at the "push of a button". Additionally, automated strict results-checking methods should be in place to prevent results from changing without the tester being quickly alerted.

With this process in place, the user of the code can be assured that the tool they are using is one that is actually capable of solving the problem at hand.

Organization of the document Chapter 2 provides the features of CTF.

Chapter 3 gives an overview of the experiments that were used for the validation study. Emphasis is placed on a brief overview of the design of the tests and their purpose as well as how CTF was used to model the tests.

Chapter 4 provides the analysis of the CTF simulations of the tests. The chapter is organized by the general effect that is being tested by the code, which include pressure drop, void content, Departure from Nucleate Boiling (DNB), turbulent mixing and void drift, and heat transfer. Some effects have multiple sets of data to compare against (e.g. pressure drop measurements were made in both BWR Full-size Fine-mesh Bundle Tests (BFBT) and FRIGG test facilities). It's important to note that the tests discussed in this section are not truly separate effects tests. For example, the void content that is compared to in Section 4.3 is not only a result of the boiling heat transfer model in CTF (which leads to void creation), but rather, it is a combination of effects like void drift, turbulent mixing, and interfacial heat transfer. Rather, the effects grouping is merely an organizational scheme that groups different test measurements and comparisons into general categories that should aid the reader in assessing the code's capabilities.

CHAPTER 2

CODE FEATURES

The basic modeling and simulation features of CTF are presented in this chapter. They are presented simply as two tables, Tables 2.1 and 2.2. Two tables are used since CTF is really like two codes in one; solid modeling and fluid modeling. The first column presents the feature. The second column presents a section number that points to where, in this document, the feature is used. Some features do not have a corresponding section number and, rather, have a dash in the column. This means that the feature has not been used in a way that would impact testing results during validation testing. It does not mean they were not exercised during this testing (or in our regression testing suite). An example of this is the rod conduction equations. While we did use the conduction models in tests like the CE 5x5 and the Harwell tube, the rod surface temperature results, which we compared to experimental values, did not depend on those models.

Another symbol that is utilized is the asterisk. The features with asterisks in their columns (i.e. "*" for the closure relations, "**" for the steam tables, and "***" for the numerical solvers) were also not explicitly tested by comparing results to known values, but they were utilized in all tests. For example, the inter-phase drag model is used for all models in this validation study. The effect is always there, though it will be more significant in some tests (e.g. DNB tests) compared to others (e.g. single-phase natural circulation). Despite the model always being on, we do not explicitly test that individual model for correctness; we test other Quantity of Interest (QOI)s that will be impacted by that model.

Speaking to the steam tables ("**"), they are used for all simulations, as no external steam tables are provided to the code, but we do not validate the individual functions that return values of subcooled liquid specific heat, superheated vapor conductivity, etc. However, we do test those individual functions as part of our unit testing procedure, which is a more appropriate place to validate such correlations. Finally, there are the numerical solvers ("***"). The Gauss-Siedel solver is used in every model to solve the momentum equations. The direct solver is used in every simulation for the conduction equation solver, and also for some simulations to solve the pressure matrix. The BiCGstab solver is used to solve the pressure matrix in some of the simulations (where the direct Gauss solver is not used). Again, these solvers are not explicitly tested in this

Table 2.1: CTF features for solids modeling

Feature	Tested in Section	Documented in Section
Solid Conduction		
Radial conduction	—	6.2
Axial conduction	—	6.2
Azimuthal conduction	—	6.2
Solid-Fluid Heat Transfer		
Single-phase convective	4.6	4.4.5
Subcooled/Saturated boiling	4.6	4.4.6
Transition boiling	—	4.4.8
Inverted annular film boiling	—	4.4.9
Dispersed droplet film boiling	—	4.4.10
Thermal radiation	—	4.4.11
Droplet impingement	—	4.4.12.1
Critical heat flux	4.4	4.4.2
Fuel Performance		
Mesh refinement	—	6.3
Pellet cracking/sintering	—	6.4.2
Pellet clad contact	—	6.4.5
Gap gas conductance	—	6.4.3
Clad-water reaction	—	6.4.6
Fuel deformation	—	6.4.2
Other solid modeling features		
Tube and solid rod heated geometry	—	6.2
Unheated conductors	—	6.2
Solid material properties	—	8.4

document. A more appropriate place for such testing would be in verification testing and unit testing. Also, when we employ PETSc to solve as our BiCgstab solver, we rely on the testing methods of the developers of that Third-Party Library (TPL).

The third column in the tables represents the section number (in the Theory Manual[9]) where the feature is documented.

Table 2.2: CTF features for fluids modeling

Feature	Tested in Section	Documented in Section
Governing equations		
Separated flow	4.2	2.2
	4.3	
	4.4	
	4.5	
	4.6	
Droplet field	4.4	2.2
Non-condensable gas	—	2.2
Closure relations		
Wall drag	*	4.2
Inter-phase drag	*	5.1
Inter-phase heat transfer	*	5.2
Droplet entrainment/de-entrainment	4.4	5.3
Turbulent mixing	4.2	4.5
	4.3	
	4.5	
	4.6	
	4.7	
Void drift	4.2	4.5
	4.3	
	4.5	
	4.6	
	4.7	
Fluid steam tables	**	8.2.1
Numerical Solvers		
Direct solver	***	2.4
Gauss-Siedel	***	2.4
BiCGstab	***	2.4
Geometry		
Multi-axial-section models	—	—
Channel splitting and coalescing	—	—
Variable axial meshing	4.2	—
	4.3	
	4.4	
	4.5	
	4.6	
	4.4	
Flow area variations	—	—

CHAPTER 3

TEST DESCRIPTIONS

This chapter presents an overview of all experiments that were used for CTF validation work. A separate section is dedicated to the description of each set of tests.

3.1 PSBT

The PWR Sub-channel and Bundle Tests (PSBT) experiments include both single-channel and rod-bundle geometries as well as steady state and transient operating conditions. The PSBT Specifications[1] organizes the experiments into two phases with different subcategories.

- Phase I: Void Distribution Benchmark
  - Exercise 1: Steady-state single subchannel benchmark
  - Exercise 2: Steady-state bundle benchmark
  - Exercise 3: Transient bundle benchmark
  - Exercise 4: Pressure drop benchmark
- Phase II: DNB Benchmark
  - Exercise 1: Steady-state fluid temperature benchmark
  - Exercise 2: Steady-state DNB benchmark
  - Exercise 3: Transient DNB benchmark

Tests from Phase I, Exercises 2 were utilized for these validation cases. Specifically, Test Series 5, 6, and 7 were used for CTF validation activities in this document. All of these test cases were rod-bundle geometry, with slightly different configurations. These configurations are

Item	Data		
Assembly	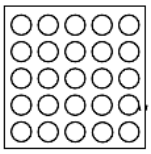 B5	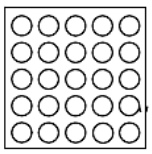 B6	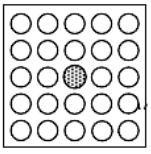 B7
Rods array	5×5	5×5	5×5
Number of heated rods	25	25	24
Number of thimble rods	0	0	1
Heated rod outer diameter (mm)	9.50	9.50	9.50
Thimble rod outer diameter (mm)	-	-	12.24
Heated rods pitch (mm)	12.60	12.60	12.60
Axial heated length (mm)	3658	3658	3658
Flow channel inner width (mm)	64.9	64.9	64.9
Radial power shape	A	A	B
Axial power shape	Uniform	Cosine	Cosine
Number of MV spacers	7	7	7
Number of NMV spacers	2	2	2
Number of simple spacers	8	8	8
MV spacer location (mm)	471, 925, 1378, 1832, 2285, 2739, 3247		
NMV spacer location (mm)	2.5, 3755		
Simple spacer location (mm)	237, 698, 1151, 1605, 2059, 2512, 2993, 3501		

Figure 3.1: Summary of PSBT rod-bundle configurations for CTF validation activities

detailed in Figure 3.1. Main differences included the power shapes and the placement of a central unheated guide tube in Assembly B7. Test Series 5 used the B5 configuration, Test Series 6 used the B6 configuration, and Test Series 7 used the B7 configuration.

The two radial power profile shapes given in Figure 3.1 are shown in Tables 3.1 and 3.2. The specification[1] provides an axial power profile table to be used to represent the cosine power shape, which is given in Table 3.3.

There are three types of spacer grids contained within the PSBT B5 bundle. There are 7 Mixing Vane (MV) spacers, 2 Non-Mixing Vane (NMV) spacers, and 8 simple spacers. Spacer grid locations are shown in Figure 3.1. The grids were modeled using the loss-coefficients provided in the PSBT specification[1]; the simple spacers had a loss coefficient of 0.4, the NMVs had a loss coefficient of 0.7, and the MVs had a loss coefficient of 1.0.

Between the three test series selected for validation studies, over 200 experiments were run as part of the experiments. For this validation work, only the cases with open, publically available data were used, which results in 35 tests being used. The test names are summarized in Table 3.4.

Operating conditions for the three tests series are given in Tables 3.5, 3.6, and 3.7.

Table 3.1: PSBT power distribution A

0.9403	0.9403	0.9403	0.9403	0.9403
0.9403	1.1062	1.1062	1.1062	0.9403
0.9403	1.1062	1.1062	1.1062	0.9403
0.9403	1.1062	1.1062	1.1062	0.9403
0.9403	0.9403	0.9403	0.9403	0.9403

Table 3.2: PSBT power distribution B

0.9838	0.9838	0.9838	0.9838	0.9838
0.9838	1.1574	1.1574	1.1574	0.9838
0.9838	1.1574	0.0000	1.1574	0.9838
0.9838	1.1574	1.1574	1.1574	0.9838
0.9838	0.9838	0.9838	0.9838	0.9838

Table 3.3: PSBT Cosine Axial Power Profile

	node	**ratio**
(Bottom)	1	0.42
	2	0.47
	3	0.56
	4	0.67
	5	0.80
	6	0.94
	7	1.08
	8	1.22
	9	1.34
	10	1.44
	11	1.51
	12	1.55
	13	1.55
	14	1.51
	15	1.44
	16	1.34
	17	1.22
	18	1.08
	19	0.94
	20	0.80
	21	0.67
	22	0.56
	23	0.47
(Top)	24	0.42

Table 3.4: PSBT tests modeled for the CTF validation study

Series 5	Series 6	Series 7
51221	61121	71121
51222	61122	71122
52111	61451	71341
52112	61452	71342
52332	62441	72221
52442	62442	73121
53441	63452	73451
53442	64561	73452
54562	64562	74561
56321	66561	74562
56322	66562	76321
56552		76322

Table 3.5: PSBT Test Series 5 Boundary Conditions

Run	**Pressure**	**Mass Flux**	**Power**	**Inlet Temperature**
-	MPa	kg/(m^2-hr)$\times 10^{-6}$	kW	°C
51221	16.50	11.00	3000	292.3
51222	16.50	10.98	2998	297.3
52111	14.53	15.08	3296	291.9
52112	14.52	14.98	3294	296.8
52332	14.69	7.94	2523	287.8
52442	14.71	4.99	2000	263.0
53441	12.28	5.00	2014	247.9
53442	12.27	5.00	2013	257.7
54562	9.83	2.02	1016	214.3
56321	4.82	7.87	3000	173.5
56322	4.81	7.86	3000	183.6
56552	4.92	2.00	1028	159.1

Table 3.6: PSBT Test Series 6 Boundary Conditions

Run	**Pressure**	**Mass Flux**	**Power**	**Inlet Temperature**
-	MPa	kg/(m^2-hr)$\times 10^{-6}$	kW	°C
61121	16.43	15.16	3372	301.5
61122	16.43	15.17	3376	306.7
61451	16.58	5.20	1914	267.4
61452	16.58	5.20	1915	272.5
62441	14.71	5.16	2415	223.5
62442	14.71	5.12	2412	228.4
63452	12.28	5.00	1920	262.5
64561	9.85	2.05	973	192.6
64562	9.85	2.05	972	213.0
66561	4.94	2.02	979	144.0
66562	4.94	2.00	979	158.5

Table 3.7: PSBT Test Series 7 Boundary Conditions

Run	**Pressure**	**Mass Flux**	**Power**	**Inlet Temperature**
-	MPa	kg/(m^2-hr)$\times 10^{-6}$	kW	°C
71121	16.42	15.07	3385	301.8
71122	16.42	15.07	3384	306.8
71341	16.55	7.92	2391	289.4
71342	16.55	7.94	2391	295.3
72221	14.64	11.01	3503	272.1
73121	12.13	15.20	3502	276.1
73451	12.27	5.03	2023	242.8
73452	12.27	5.03	2021	260.1
74561	9.83	2.16	1023	196.8
74562	9.84	2.16	1023	214.9
76321	4.89	8.10	3541	153.5
76322	4.87	8.06	3536	168.6

The average void in the four channels surrounding the central rod was the measured quantity of interest in the steady-state tests (Test Series 5, 6, and 7). These measurements were made via X-ray densitometer measurements at three different axial locations; 2.216 m, 2.269 m, and 3.177 m from Beginning of Heated Length (BOHL). The estimated accuracy of the void fraction measurements was 4% void. Additional information on bundle manufacturing tolerances as well as operating condition uncertainties are given in the test specifications.

3.2 BFBT

Like the PSBT tests, the BFBT tests are organized into phases and exercises in the BFBT specification[2].

- Phase I: Void Distribution Benchmark
  - Exercise 1: Steady-state subchannel grade benchmark
  - Exercise 2: Steady-state microscopic grade benchmark
  - Exercise 3: Transient microscopic grade benchmark
  - Exercise 4: Uncertainty analysis of the void distribution benchmark
- Phase II: Critical Power Benchmark
  - Exercise 0: Steady-state pressure drop benchmark
  - Exercise 1: Steady-state critical power benchmark
  - Exercise 2: Transient benchmark

Currently, the validations cases within CTF include Exercise 0 from the BFBT Phase 2 benchmark. Specifically, these cases cover pressure drop measurements and quality calculations for single- and two-phase flow through the test bundle. The names of these two sets of tests in the specification are P6 (two-phase pressure drop measurements) and P7 (single-phase pressure drop measurements). For this validation study, 18 two-phase pressure drop (P6) experiments and 10 single-phase pressure drop (P7) experiments were modeled. Tests are summarized in Table 3.8.

Both test series used the C2A rod-bundle geometry, which is shown in Figure 3.2. This particular bundle geometry is representative of a high burn-up assembly at beggining of cycle. It is an older-style, 8×8 BWR heated rod bundle. There are 60 identical heated rods and a central unheated water rod which has no flow through its center. The radial power profile is non-uniform, as is the axial power profile, which is a cosine shape. Table 3.10 contains the radial power profile while Table 3.9 contains the axial power profile for this bundle. Pressure tap locations are shown in Figure 3.3.

There are seven spacer grids located axially at 455, 967, 1479, 1991, 2503, 3015, and 3527 mm from the bottom of the heated length. These are ferrule-type spacers which have circular tubes (ferrules) to guide each heated rod as well as the central water rod. An example of this type of grid is shown in Figure 3.5.

Table 3.8: BFBT tests modeled for the CTF validation study

Series P6	Series P7
60001	70027
60003	70028
60005	70029
60007	70030
60009	70031
60013	70032
60015	70033
60017	70034
60019	70035
60022	70036
60023	
60024	
60025	
60026	
60029	
60030	
60031	
60032	

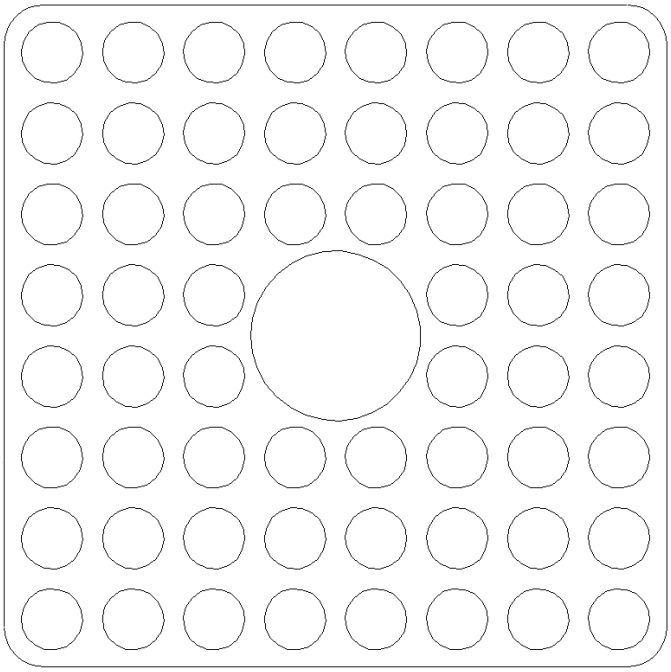

Figure 3.2: BFBT C2A bundle geometry

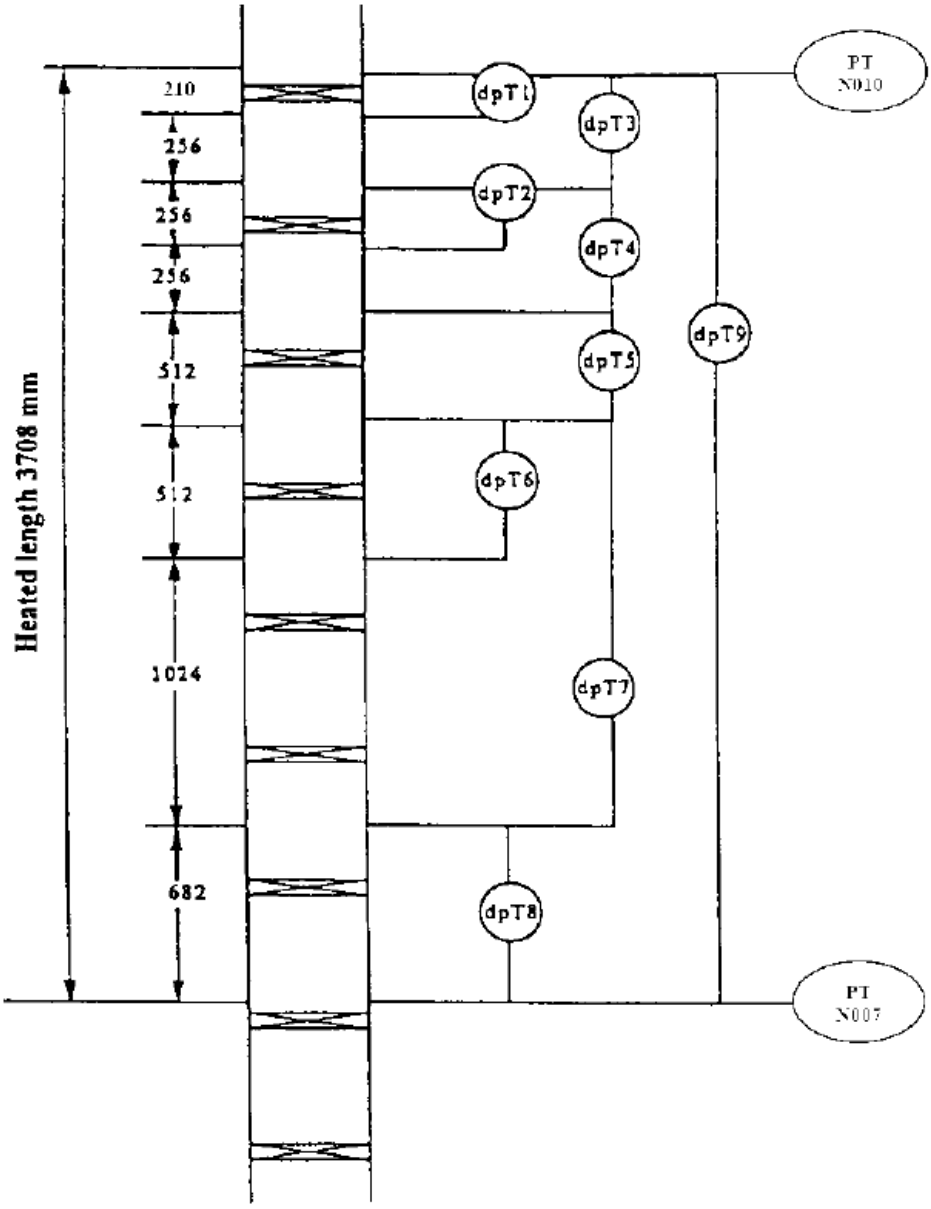

Figure 3.3: BFBT bundle pressure tap locations

Table 3.9: BFBT C2A Bundle Axial Power Distriubution

	node	**ratio**
(bottom)	1	0.46
	2	0.58
	3	0.69
	4	0.79
	5	0.88
	6	0.99
	7	1.09
	8	1.22
	9	1.22
	10	1.34
	11	1.34
	12	1.40
	13	1.40
	14	1.34
	15	1.34
	16	1.22
	17	1.22
	18	1.09
	19	0.99
	20	0.88
	21	0.79
	22	0.69
	23	0.58
(top)	24	0.46

Table 3.10: BFBT C2A Bundle Radial Power Distribution

1.15	1.30	1.15	1.30	1.30	1.15	1.30	1.15
1.30	0.45	0.89	0.89	0.89	0.45	1.15	1.30
1.15	0.89	0.89	0.89	0.89	0.89	0.45	1.15
1.30	0.89	0.89	-	-	0.89	0.89	1.15
1.30	0.89	0.89	-	-	0.89	0.89	1.15
1.15	0.45	0.89	0.89	0.89	0.89	0.45	1.15
1.30	1.15	0.45	0.89	0.89	0.45	1.15	1.30
1.15	1.30	1.15	1.15	1.15	1.15	1.30	1.15

The loss coefficients for this type of spacer grid were calculated using the approach of Shiralkar and Radcliffe[10]. This approach assumes the pressure drop over a grid to be a sum of form and friction losses, as depicted in Equation 3.1. Each of these individual components are calculated individually by Equations 3.2 and 3.3. In Equation 3.2, the orifice loss factor, k', is taken as 0.5 for a sharp orifice and σ represents the contraction ratio, or, the ratio of the cross-flow area in the grid region over the cross-flow area in the upstream, bare region. In Equation 3.3, f is the friction factor, L is the length of the grid, P_U is the upstream wetted perimeter, and P_R is the wetted perimeter in the grid spacer. The bare, upstream cross-flow area is A_U and, as in Equation 3.2, σ is the contraction ratio. The friction factor was taken to be a constant value of 0.015. The loss coefficients were individually calcualted for each subchannel using these equations. The loss coefficients for all channels are summarized in Figure 3.4.

$$K = K_L + K_f \tag{3.1}$$

$$K_L = \left[\frac{\sqrt{k' * (1-\sigma)} + (1-\sigma)}{\sigma} \right]^2 \tag{3.2}$$

$$K_f = \frac{fLP_U}{4A_U} \left[\frac{P_R}{P_U} \left(\frac{1}{\sigma} \right)^3 - 1 \right] \tag{3.3}$$

Boundary conditions for the two test series are shown in Tables 3.11 and 3.12. Estimated unceratinty for measured values are given in Table 2.4.3 of the specification.

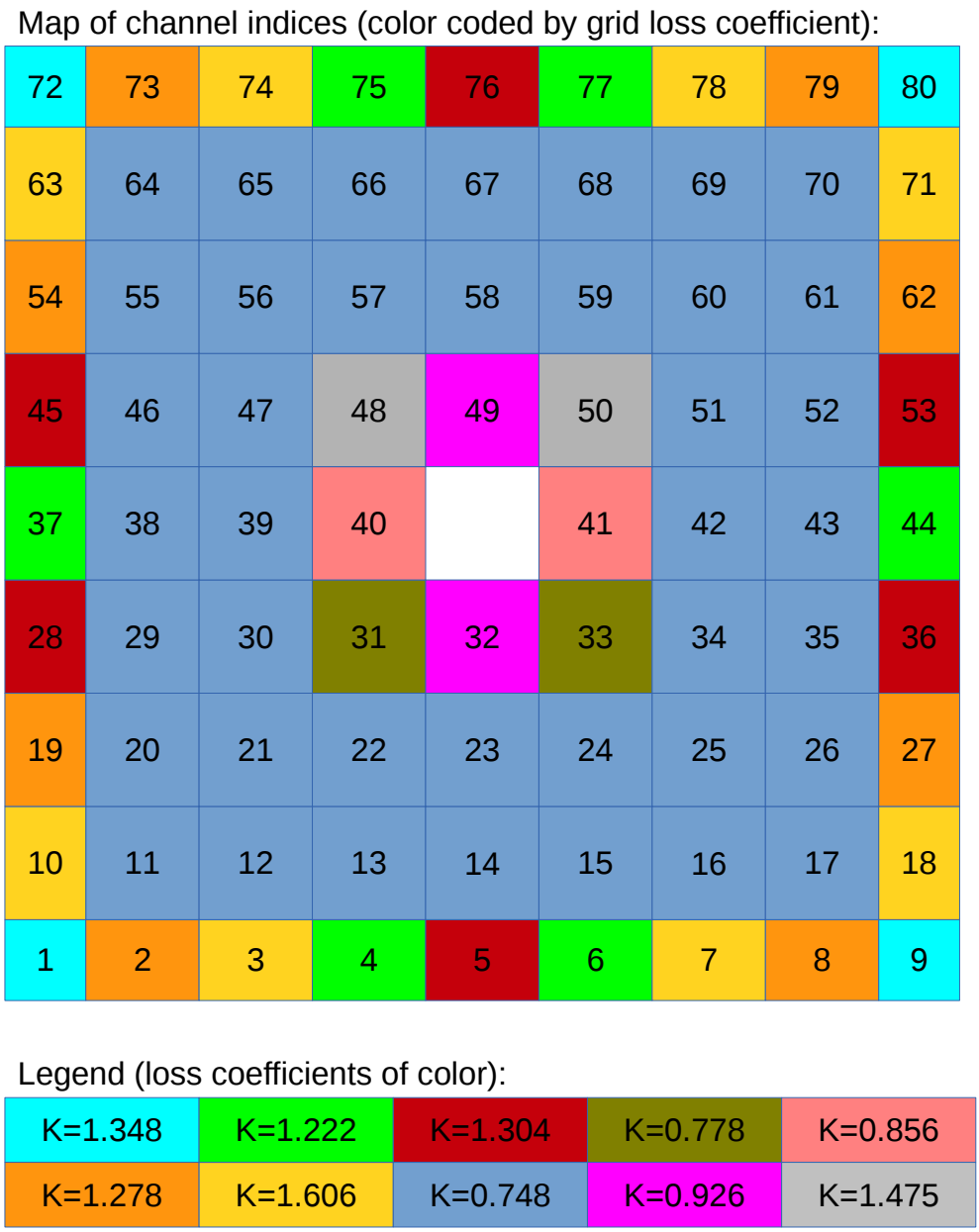

Figure 3.4: Map of channels in BFBT cases with loss coefficient for each channel as calculated by Shiralkar and Radcliffe

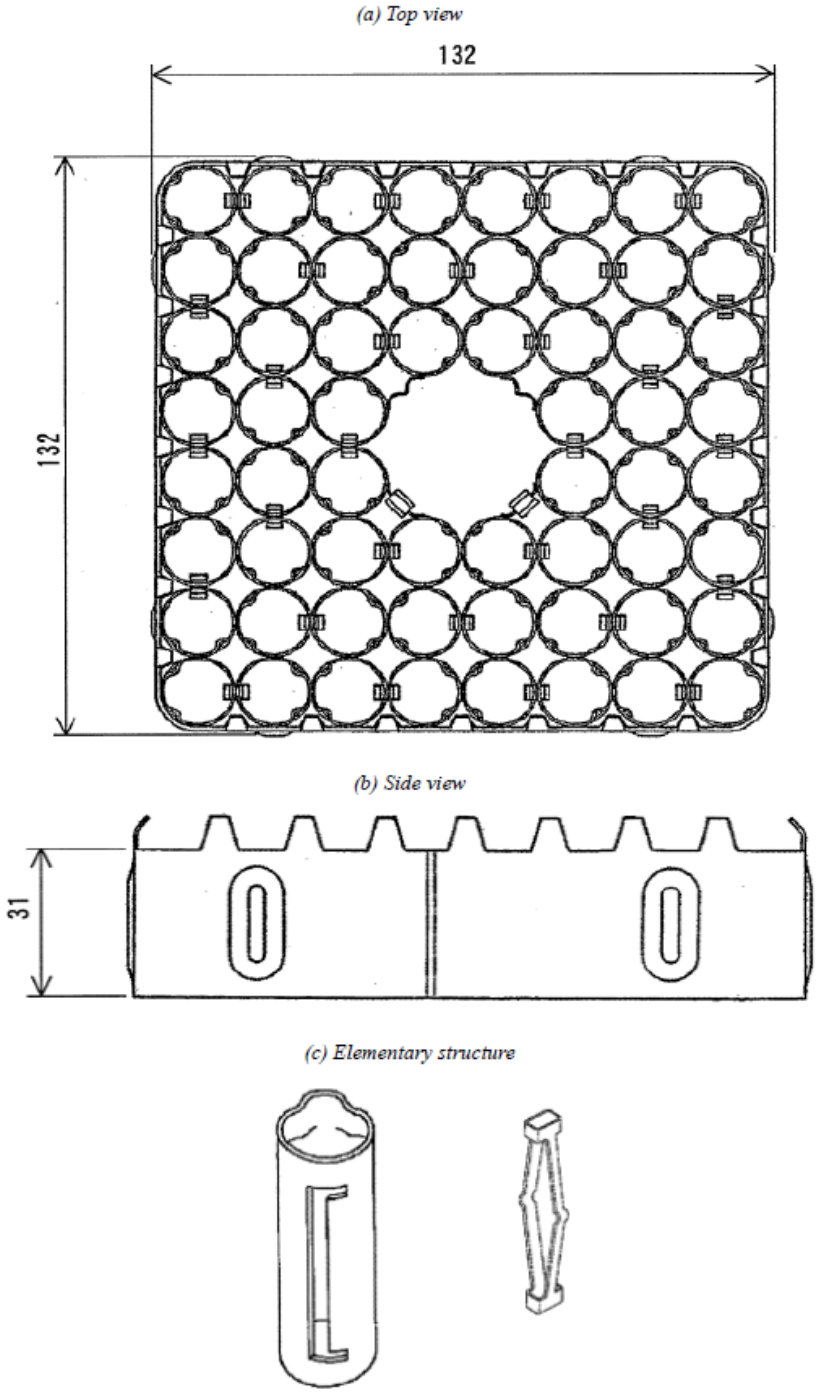

Figure 3.5: BFBT C2A Ferrule Grid Geometry (1)

Table 3.11: BFBT Series P6 Boundary Conditions

	Pressure MPa	**Inlet Temperature** °C	**Inlet Subcooling** kJ/kg	**Flow Rate** ton/hr	**Power** MW
P60001	7.16	277.3	53.3	20.2	0.863
P60003	7.16	277.8	50.8	20.1	1.521
P60005	7.16	277.7	51.1	20.0	2.357
P60007	7.17	277.8	51.1	55.0	2.375
P60009	7.17	277.8	51.1	55.0	4.197
P60013	7.16	278.4	47.2	69.9	3.022
P60015	7.17	278.2	49.5	70.0	5.340
P60017	7.16	277.8	51.0	45.1	1.919
P60019	7.17	278.2	49.4	45.0	3.437
P60022	8.64	291.3	50.7	20.2	0.837
P60023	8.63	291.0	52.3	20.2	1.464
P60024	8.63	290.9	52.9	20.2	2.252
P60025	8.64	291.3	51.3	55.0	2.271
P60026	8.64	291.0	53.0	55.1	3.975
P60029	8.64	291.3	51.5	70.1	2.888
P60030	8.64	291.2	51.4	70.2	5.076
P60031	8.64	290.9	53.0	45.1	1.869
P60032	8.63	291.2	51.3	45.2	3.262

Table 3.12: BFBT Series P7 Boundary Conditions

	Pressure MPa	**Inlet Temperature** °C	**Flow Rate** ton/hr	**Reynolds #** $\times 10^{-4}$
P70027	7.15	284.9	20.30	8.07
P70028	7.16	285.1	24.90	9.91
P70029	7.16	285.1	29.80	11.86
P70030	7.16	285.7	34.70	13.82
P70031	7.16	285.6	39.70	15.81
P70032	7.16	285.3	44.60	17.75
P70033	7.15	284.7	55.00	21.86
P70034	7.15	284.8	59.70	23.74
P70035	7.16	284.6	64.80	25.76
P70036	7.15	284.8	69.90	27.79

3.3 PNNL 2x6

These two experiments, both made in a 2-by-6 apparatus with the same geometry, were meant to provide benchmark data to evaluate the ability of codes to account for the effects of buoyancy on flow patterns. They contained fixed inlet flow, which was then re-distributed across the bundle by temperature gradients due to differing powers on the two sides. Specifically, for both problems, three rows of heater rods on one side were given power, while those on the other side were unheated. The apparatus contained 9 windows at 6-inch intervals along its 4-ft heated length. At these elevations, a Laser Doppler Anemometer (LDA) was used to measure velocities along lines at 3 locations (Y = -0.581, 0.0, 0.581), which correspond to the three subchannel rows along the 2-rod dimension. Additionally, thermocouple measurements were made in several subchannel centers at these same elevations.

The CTF model contained 12 rods and 21 subchannels arranged as shown in Figure 3.6. The numbering from the steady-state test reference[7] was used, in contrast to that in the transient test reference[3], where the subchannel numbering began in the middle row. The axial meshing of the test section is shown in Figure 3.7. Pertinant geometric information can be found in Table 3.13.

Along with the 4 ft heated length of the rods, 6 inches of unheated length above and below were included. There were a total of 30 axial nodes, each 2 inches long. The second friction option was used (irfc=2), as well as the Rogers and Roseheart single-phase mixing coefficient (imix =2). As these are both single phase cases, options for liquid entrainment, two-phase mixing, and void drift were turned off or set as the defaults.

The steady-state problem was modeled using the boundary conditions found in Table 3.14. The transient problem had the boundary conditions shown in Table 3.15. However, note that convergence problems were experienced for the low pressure of the case, so the pressure was increased to 60 psi for the transient case. Since the test contained single-phase liquid and low temperature, it is anticipated this change to pressure will have an insignificant impact on results. Additionally, to ensure the case started at steady state, the transient flow ramp was not started until 300 seconds in the CTF simulation.

Table 3.13: Subchannel geometry data for the PNNL 2x6 facility

Parameter	Value
Rod diameter	0.475 in
Rod pitch	0.575 in
Rod-wall spacing	0.350 in

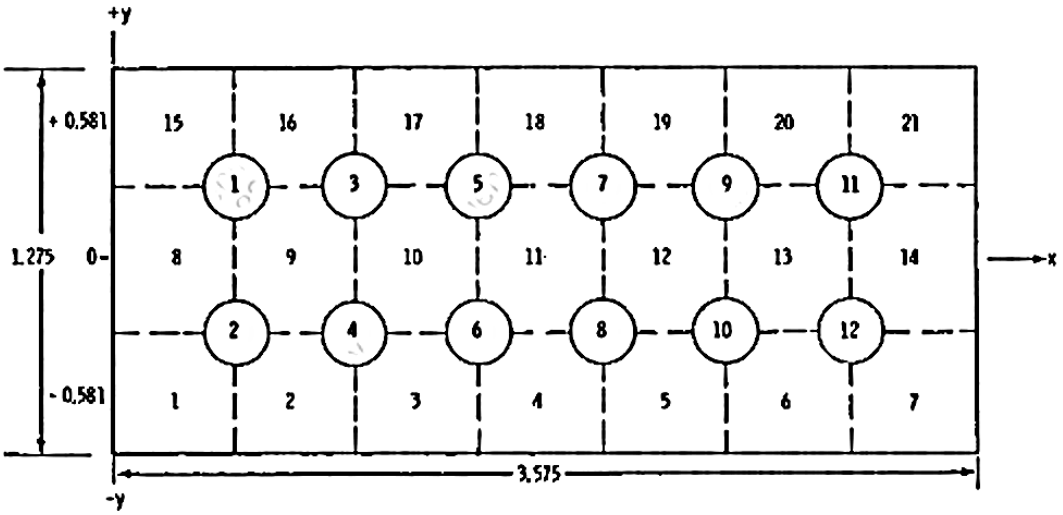

Figure 3.6: Cross-sectional geometry of the PNNL 2x6 test section

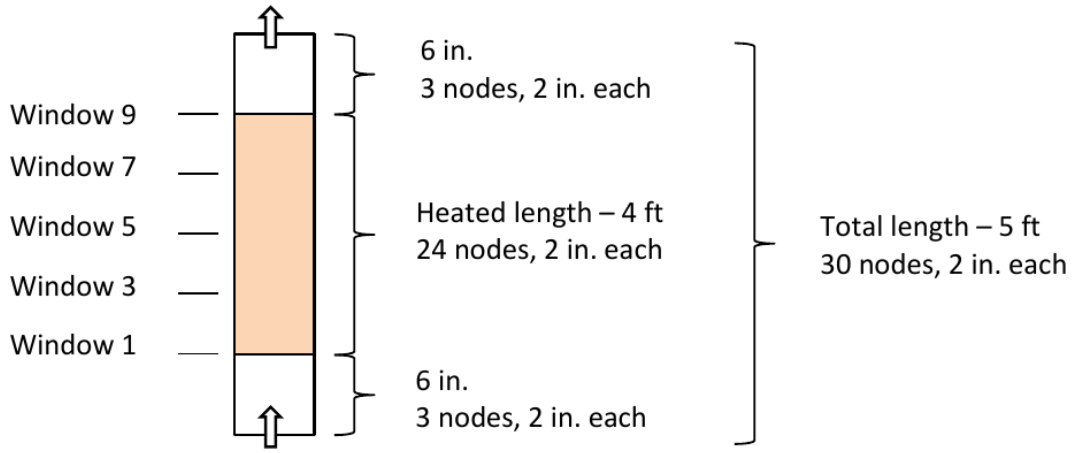

Figure 3.7: Axial schematic of the PNNL 2x6 facility and CTF meshing

Table 3.14: Boundary conditions for PNNL 2x6 steady-state test

Pressure (psi)	60
Inlet temperature (F)	60.6
Outlet temperatuer (F)	93.1
Flow rate (gpm)	1.25
Power per rod [kW]	0.91

Table 3.15: Boundary conditions for PNNL 2x6 transient test (Case 22)

Pressure (psi)	20
Inlet temperature (C)	22.9
Outlet temperature (C)	67.8
Initial flow rate (gpm)	1.63
Final flow rate (gpm)	0.55
Flow ramp start (s)	0.0
Flow ramp end (s)	45.0
Power per rod (kW)	0.91

3.4 CE 5x5

In the early 1980s, Combustion Engineering (CE) teamed up with Columbia University to perform rod-bundle experiments to provide insight on the efficacy of single- and two-phase heat transfer models that are typically used for predicting steaming rate and crud buildup[5]. Two 5x5 rod-bundle tests (named Test 74 and Test 75) were performed at the Columbia University Heat Transfer Research Facility, which were designed to simulate the peripheral region of adjacent CE 14x14 fuel bundles. These tests were prompted after heavy crud deposits and fuel failures were observed on peripheral rods for bundles in Maine Yankee cycle 4.

The expeirments were run at prototypical PWR pressure, temperature, and heat flux. Target operating conditions are given in Table 3.16. The rods were 7 feet in lenght and uniformly electrically heated in the axial direction; rods were non-uniformly heated in the radial direction, as shown in the cross-section diagrams of the facility in Figures 3.8 and 3.9. The grids contained no mixing vanes. Thermocouples were placed at four axial locations in both the central heater tube and one adjacent heater tube. Additionally, pressure maeasurements were made via four pressure taps. Figure 3.10 shows a simple axial diagram of the assembly.

Pressure drop measurements were made at cold conditions (80 F and 130 F) at a pressure of 1000 psia. The inlet mass velocity was varied such that Reynolds-dependant grid-loss correlations could be developed. The Moody friction factor correlation was used to characterize the frictional component of pressure drop. The grid loss coefficients were calculated by the authors on a per-subchannel basis considering the blockage ratio and wetted perimeter of each subchannel (see Table 5.1 of specification[5]). These loss coefficients were used in the CTF model.

Heated tests were run at a wide range of heat fluxes in order to cause single-phase, subcooled boiling, and saturated boiling regions of the boiling curve in the upper assembly. Transition to boiling was detected by observing a "levelling-off" of the rod surface temperature with increasing heat flux. Additionally, several DNB tests were performed by ramping up the power in the facility until a sharp temperature increase was detected at the thermocouple locations, indicating a post-CHF heat transfer regime has been entered. CHF results are presented in Table 3.17.

Table 3.16: Target operating conditions for CE 5x5 Tests 74 and 75

Inlet Temperature (F)	Pressure (psia)	Mass Velocity (Mlbm/hr-ft^2)
564	2250	2.25
583	2250	2.25
543	2250	2.97
512	1750	2.25

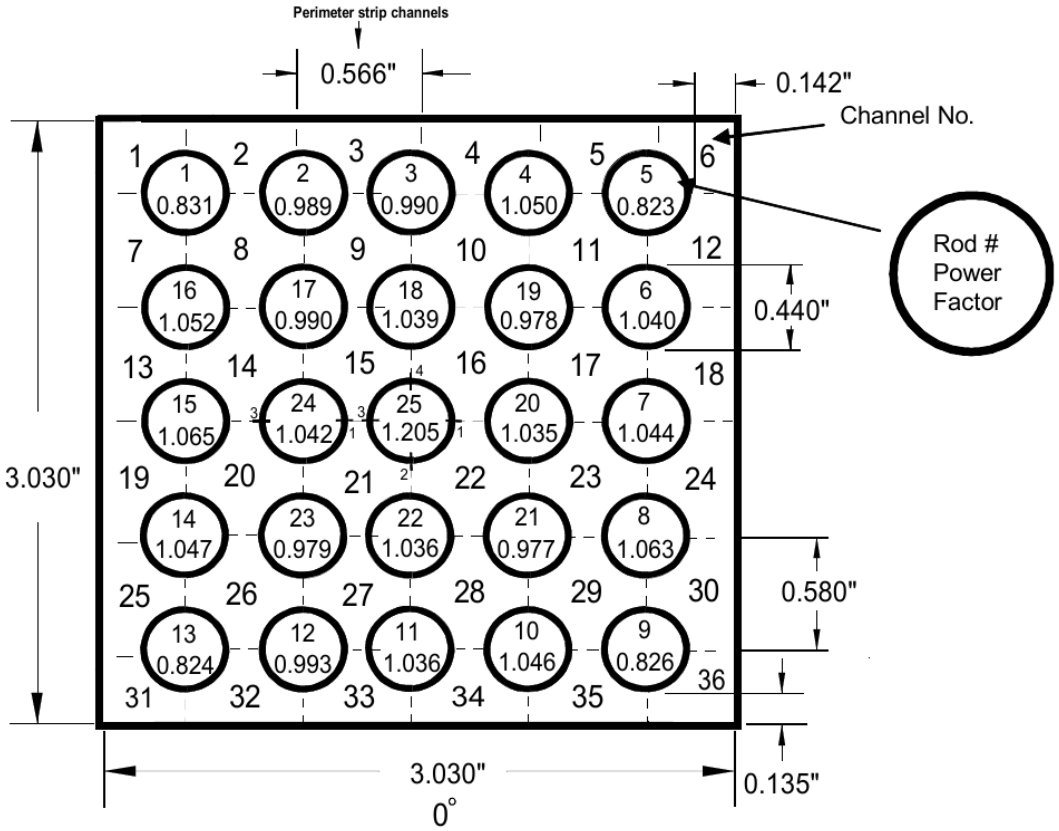

Figure 3.8: Cross-section diagram of CE 5x5 Test 74

Table 3.17: CHF results for CE 5x5 Tests 74 and 75

Test	Inlet Temperature (F)	Pressure (psia)	Mass Velocity (Mlbm/hr-ft^2)	Rod CHF (MBTU/hr-ft^2)	T/C CHF Location (in)
74	562.5	2254.7	2.259	0.652	25.43
74	545.7	2254.7	2.236	0.697	25.43
74	514.0	1749.7	2.203	0.695	25.43
					25.41
74	582.0	2254.7	2.964	0.718	25.43
75	563.5	2249.7	2.281	0.679	25.43
75	547.5	2249.7	2.211	0.708	25.43
75	516.0	1749.7	2.224	0.715	25.43
					25.41
75	584.0	2249.7	2.927	0.743	25.43

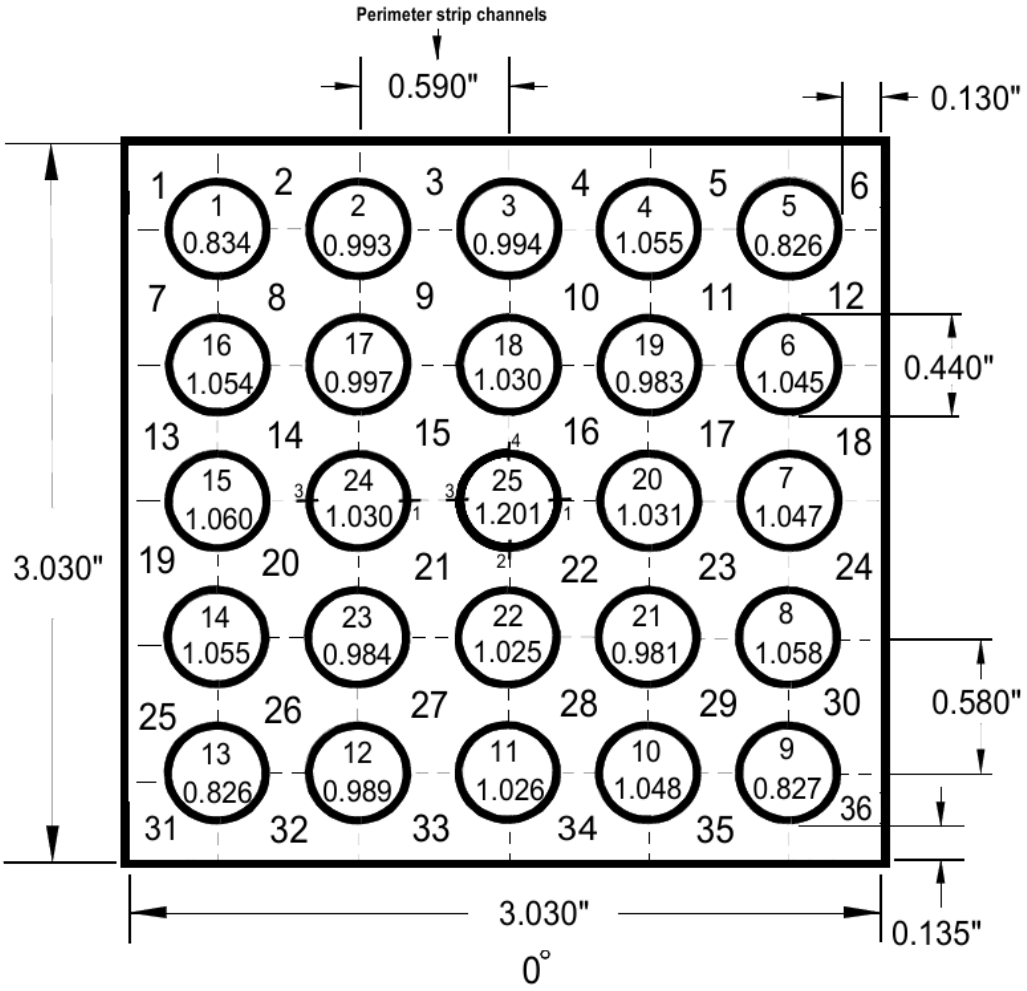

Figure 3.9: Cross-section diagram of CE 5x5 Test 75

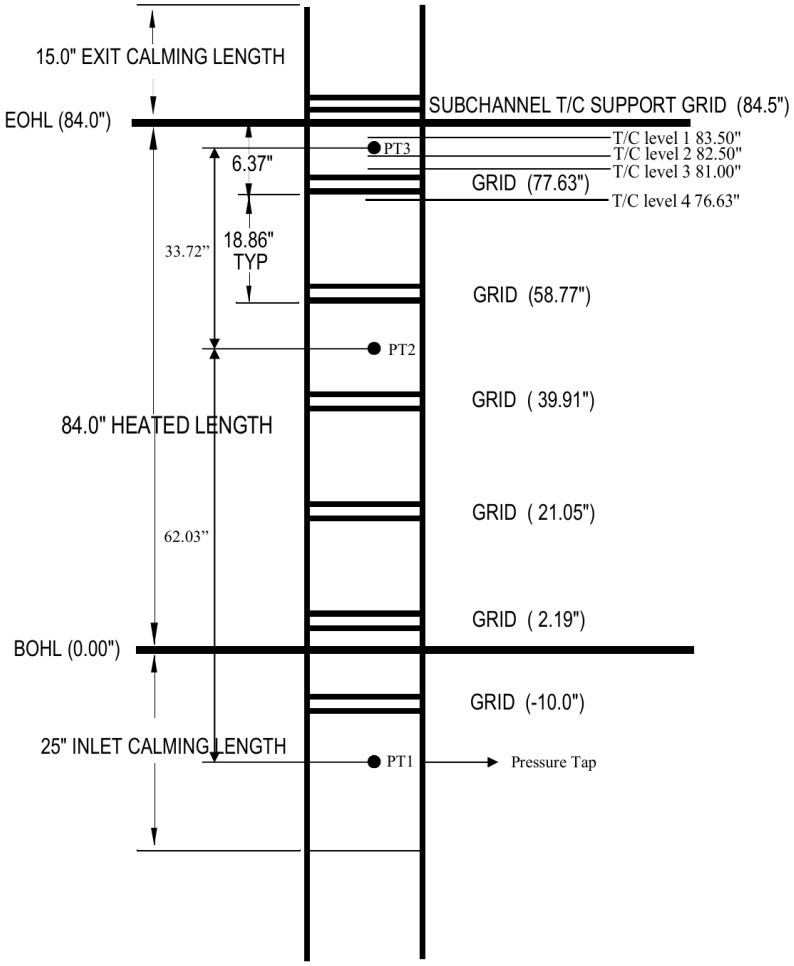

Figure 3.10: Axial schematic of the CE 5x5 bundle

3.5 GE 3x3

A 3×3 heated tube geometry was used in a BWR-like simulation with GE rods[8]. The geometry of the bundle is shown in Figure 3.11. The details of this bundle are provided in Table 3.18. A summary of the geometry of the 16 subchannels is provided in Table 3.19.

The axial and radial power profiles were uniform for all of these test cases. The same bundle was used for all the tests as well. The differences are in the power, flow rate, and inlet subcooling.

Subchannel measurements were taken to determine the specifics of coolant flow through different types of subchannels. The target parameters were the flow rate and the enthalpy as compared to the bundle-averaged values. The 2B and 2D series test cases all utilize a uniform radial and axial heat flux distribution. The main difference between the two series is the power level. The subcooling is specified as well, as is shown in Table 3.20.

There are pins holding the rods in place which act as spacers. These pins are 3.18 mm in diameter and either 3.43 mm long or 4.27 mm long, for either rod-rod or rod-wall connections, respectively. There are four pins connected to each rod spaced evenly azimuthally and perpendicular to the shroud surface where they connect. These locations are along the subchannel boundaries which are indicated in Figure 3.12. Pins labeled with either 'A' or 'B' are 3.43 mm in length, while pins labeled with either 'C' or 'D' are 4.27 mm in length. All pins have the same diameter: 3.18 mm. These pins were fusion-welded to the outside of each pin and to the walls.

There are six sets of 24 pins spaced every 304.8 mm starting 50.8 mm from the bottom of the heated length. The locations of these six pin spacers are 50.8, 355.6, 660.4, 965.2, 1270.0, and 1574.8 mm from the bottom of the heated length.

The quantities of interest for predicted to experimental comparison are:

- Normalized subchannel mass flux versus bundle-averaged quality
- Normalized subchahnel enthalpy versus bundle-averaged quality

The measurements taken during the experiment were mass flows and enthalpies of specific subchannels. These were grouped by subchannel type: corner, side, or center. The subchannels

Table 3.18: GE 3×3 Bundle Description

Item	Description
Number of heater rods	9
Heater rod OD (mm)	14.5
Heated length (mm)	1828.8
Rod pitch (mm)	18.7
Channel box inner width (mm)	58.83
Channel box corner radius (mm)	10.2
Flow area (mm^2)	1890.3
Number of spacers	6
Spacer type	Pin

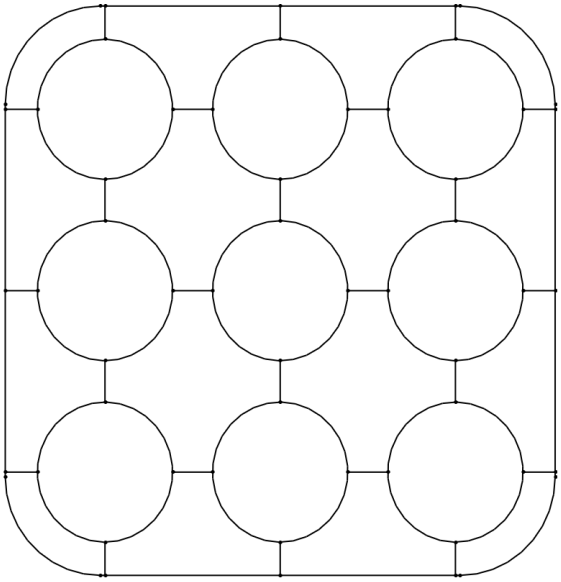

Figure 3.11: GE 3×3 Bundle Geometry

Table 3.19: GE 3×3 Bundle Subchannel Geometry

	Area m^2	**Wetted Perimeter** m
Corner	5.050E-05	2.835E-02
Side	1.177E-04	4.149E-02
Center	1.868E-04	4.548E-02
Bundle	*1.890E-03*	*6.272E-01*

Table 3.20: GE 3×3 Bundle Boundary Conditions by Test Series

Test Series -	**Power** kW	**Bundle-averaged Flow Rate** kg/s	**Inlet Subcooling** kJ/kg
2B2	532	1.360	348.4
2B3	532	1.373	252.6
2B4	532	1.373	122.7
2C1	*532*	*2.720*	*132.9*
2C2	*532*	*2.740*	*81.57*
2D1	1064	1.386	602.4
2D3	1064	1.386	289.1
2E1	*1064*	*2.771*	*332.1*
2E2	*1064*	*2.771*	*224.7*
2E3	*1064*	*2.712*	*67.63*
2E1	1064	2.771	332.1
2E2	1064	2.771	224.7
2E3	1064	2.712	67.63
2G1	*1596*	*2.746*	*525.0*
2G2	*1596*	*2.771*	*441.1*
2G3	*1596*	*2.746*	*340.9*

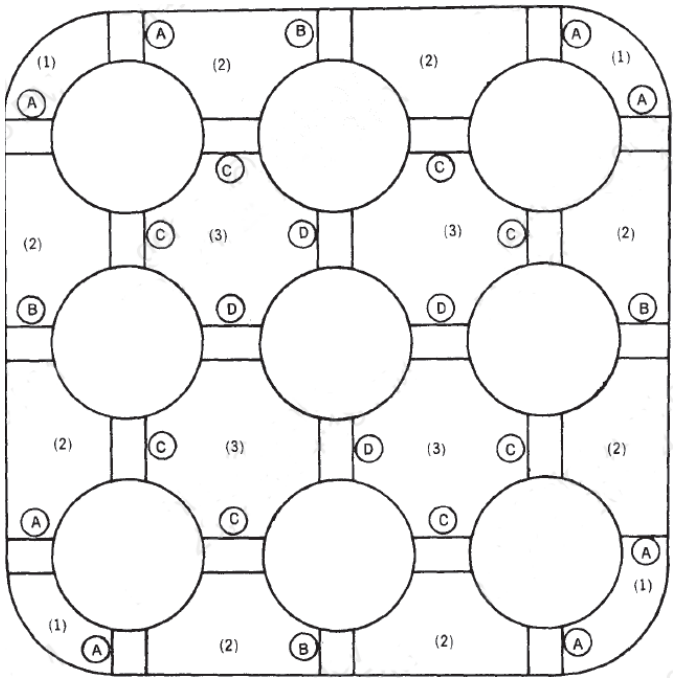

Figure 3.12: GE 3×3 Bundle Pin Spacer Geometry

were isolated using special ducting in order to obtain measurements at only the subchannel type of interest. Once isolated using sheets of metal, the flow rate and enthalpy of the fluid passing through the subchannel are measured using a turbine flowmeter (for the flow) and by a heat balance on a calorimeter (for the enthalpy). Pressure loss values were also measured using pressure transducers across the entire bundle [8].

The normalized subchannel mass flux and enthalpy is calculated for each of the three types of subchannels in this bundle. They are normalized in order to gain a comparison of that particular subchannel's flow or enthalpy to that of the entire bundle as a whole. The flow normalization is performed by Formula (3.4). Similarly, the enthalpy normalization is performed as shown in Formula (3.5).

$$\frac{G_{ch} - \overline{G}}{\overline{G}} \tag{3.4}$$

$$\frac{H_{ch} - \overline{H}}{\overline{H}} \tag{3.5}$$

In these equations, $\overline{G}$ and $\overline{H}$ correspond to the bundle-averaged values of flow rate and enthalpy, respectively, and G_{ch} and H_{ch} are the flow rate and enthalpy of the subchannel type.

3.6 Harwell High Pressure Loop

Post-dryout (post-CHF) experiments were performed in the Harwell High Pressure Two-Phase Heat Transfer Loop facility[4]. The facility consisted of an electrically heated tube with water flowing in the inside. The tube had a 0.496 inch inner diameter, was 19 ft long, and was vertically aligned. Thermocouples were affixed to the outside of the tube, the spacing being as large as 12 inches and as small as 3 inches near the top of the test section. A series of tests were performed where the flow conditions were such that dryout occured at some location in the tube. This was achieved by adjusting inlet flow rate and test section power; the outlet pressure was fixed at 1000 psi for all tests.

The testing procedure involved increasing the power until a sharp temperature increase was detected, indicating that dryout had occurred. Measured temperatures were used to calculate the tube inside surface temperatures, which were summarized for all tests in the report by Bennett, et al.[4].

Two varieties of tests were performed; one with a 144 inch active length and another with a 219 inch active length. Only the 219 inch active length tests were modeled in CTF. Therefore, the geometry and problem mesh was the same for all tests modeled. Only the flow conditions had to be varied from test-to-test. A schematic of the CTF axial mesh is shown in Figure 3.13. The CTF model consisted of one channel and one heater tube. The model was setup as if the flow was on the exterior of the heater tube. The outer diameter of this tube was set equal to the inner tube diameter so that the tube surface area of the rod/fluid interface was consistent with the experiments. The channel flow area and wetted perimeter in the CTF subchannel was set equal to the flow area of the inside of the tube. Only the active region of the experiment was modeled. The axial meshing was done such that the center of the CTF mesh cells were within 4 mm of the actual measurement location in the experiment.

The axial mesh is laid out in groups of cells all having the same height. In the figure, the green block on the bottom denotes a group of cells having 4 inch heights. From 112 inches and up, the mesh is gradually made more refined. The blue block represents a region where mesh cell size is 0.5 inches. This was done because this region (112 inches and up) is where dryout occurs, which requires a finer mesh. With the way the mesh was setup, the axial locations of test facility thermocouples always lines up with a CTF cell center.

Due to the inclusion of the droplet field entrainment/de-entrainment and the complex physics being modeled, it was difficult to converge these tests to a level of tolerance communseratue with that of simpler, single-phase tests. Therefore, the minimum and maximum allowable timestep sizes were set to 1E-7 s and 1E-4 s, respectively and the ratio between the conduction and fluid solution time scales was set to 1.0 (a value we normally increase to 10,000). Even with these extra measures, it was tpically only possible to drop the mass and energy storage terms to about 0.1–1%. Mass and energy balance terms were generally more well behaved, dropping to 0.001–0.01%.

Boundary conditions were set to match experimental values; a pressure boundary condition was set at the test outlet and a mass flow rate and enthalpy boundary condition was set at the inlet. The author provided inlet subcooling as a boundary condition, so the tests were run in an iterative fashion to match the inlet subcooling to experimental values. The tube material properties were set to that of Zircaloy, though this has no impact on the solution value of interest,

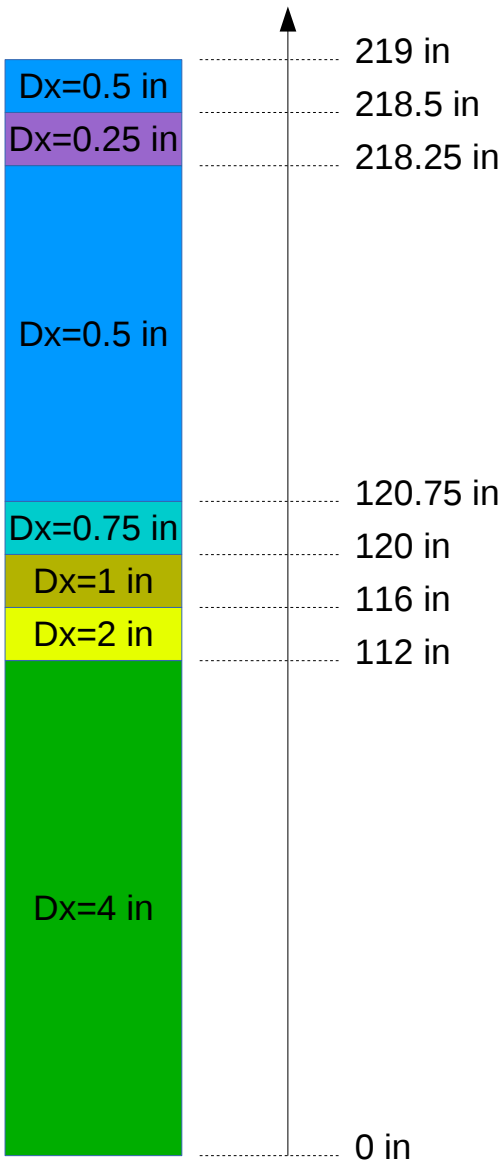

Figure 3.13: CTF model of the Harwell High-Pressure Two-Phase Test Facility

the tube surface temperature, because we run the case to steady-state, where all heat generated in the model is being deposited into the fluid.

3.7 FRIGG

The FRIGG test facility consists of an electrically heated rod bundle, modeled after the Marviken reactor assemblies[6]. Experiments were run in the facility to verify that the Marviken reactor could be run at the rated power with proper safety margins against burnout. Investigations included single- and two-phase pressure drop measurements, axial and radial void distribution measurements, and burnout in natural and forced circulation. In this study, we model a single uniformly heated, natural convection, two-phase flow test case from the study. Comparisons were made between experimental and predicted axial temperature, pressure, void, and quality profiles. Results demonstrate that all measured results were correctly predicted by CTF.

3.7.1 CTF Model of Facility

3.7.1.1 Radial Meshing

The Marviken reactor uses fuel assemblies having lattices much different than that of a typical U.S. PWR. The 36 fuel rods are situated so that their centers lie on rings of increasing size going outwards from the center of the circular shaped bundle. An unheated guide tube lies at the center of the bundle. The first ring of rods occurs at 21.6 mm from the center and contains 6 fuel rods. The second ring of rods occurs at 41.7 mm from center and contains 12 fuel rods. The third and final ring occurs at 62.2 mm from center and contains 18 rods. This leads to a total of 36 fuel rods and one central guide tube. The canister for the fuel assembly has a diameter of 159.5 mm. The gap between rods on the same ring is 7.8 mm.

Figure 3.14 shows the cross-section of the Marviken assembly (and the FRIGG test facility). The CTF modeling approach for this facility is also shown in the figure. To simplify the modeling of the facility, a lumped-subchannel approach was utilized. The space between the central guide tube and the first ring of rods formed the first subchannel in the CTF model. Likewise, the space between the first and second ring of rods formed the second subchannel, and so on. In addition to lumping the subchannels together, it also made sense to lump fuel rods and gaps, as well. The first ring of rods were lumped into Rod 2, the second ring of rods were lumped into Rod 3, and the third ring of rods were lumped into Rod 4. In this way, there were no gaps modeled in the azimuthal (θ) direction of the circle; rather, gaps only exist in the radial (r) direction. Since the rod spacing is always 7.8 mm in the θ direction, it was possible to lump all gaps on a given ring together.

To create the CTF model, it was necessary to calculate the cross-flow area of the rings as well as their wetted perimeter. Any given fuel rod resides in exactly two rings. In order to obtain the channel area and wetted perimeter, it was necessary to determine how much of the fuel rod is in each of the two rings it occupies. To do this, we first zoom in on a single fuel rod and define an equation for the circle whose circumference passes through the fuelrod center. This is shown in Figure 3.15, where the blue circle represents the fuel rod. If we assume that the large circle's

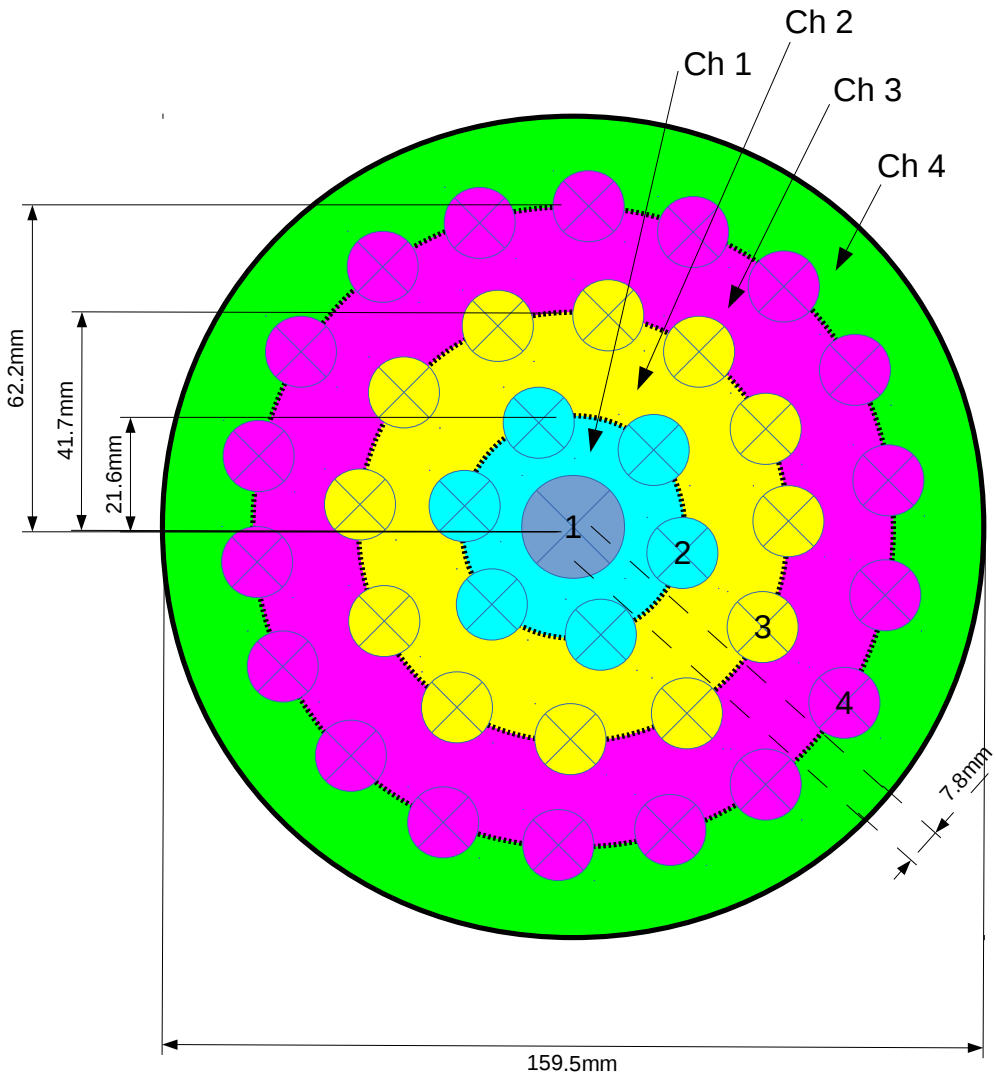

Figure 3.14: Cross-section of the FRIGG facility (including labels of CTF model rods and channels)

center is at the origin, we can define functions for both circles.

To obtain the area of the fuel rod in the smaller of the two rings, we can simply integrate the difference of the two functions that define the larger and smaller circles between their intersections. In equation form:

$$A_{\text{small}} = \int_{x_0}^{x_1} f_{\text{large circle}}(x) - f_{\text{small circle}}(x) \tag{3.6}$$

Here, A_{small} is the cross sectional area of the rod residing in the smaller channel. Substituting the actual equations of the circles leads to the following:

$$A_{\text{small}} = \int_{x_0}^{x_1} \sqrt{R^2 - x^2} - (-\sqrt{r^2 - x^2} + R) \tag{3.7}$$

Here, R is the radius of the large circle and r is the radius of the small circle that represents the fuel rod. It was assumed that the fuel-rod circle lay directly above the center of the large circle, so that its equation is simply shifted up the y axis and requires no shift in the x direction. Since the fuel-rod circle center is situated on the larger circle circumference, the fuel-rod circle equation is shifted up the y-axis by distance R. The intersection points of the two circles can be found by setting the equations equal to one another and solving for x. Since the fuel-rod circle is directly above the large circle center, the two intersection points have the same magnitude, but opposite sign:

$$x_0 = -\sqrt{r^2 - \frac{r^2}{4R^2}} \tag{3.8}$$

$$x_1 = \sqrt{r^2 - \frac{r^2}{4R^2}} \tag{3.9}$$

Doing the integration of Equation 3.7 from the bounds given in Equations 3.8 and 3.9 yields the following equation for cross-sectional area of a rod residing in the smaller channel:

$$A_{\text{small}} = \left[\frac{x}{2}\sqrt{R^2 - x^2} + \frac{R^2}{2}\sin^{-1}\frac{x}{R} + \frac{x}{2}\sqrt{r^2 - x^2} + \frac{r^2}{2}\sin^{-1}\frac{x}{r} - Rx\right]_{x_0}^{x_1} \tag{3.10}$$

The area of the rod residing in the larger channel is then simply calculated as the total rod cross-sectional area minus the smaller area given by Equation 3.10.

$$A_{\text{large}} = \pi r^2 - A_{\text{small}} \tag{3.11}$$

The channel cross-sectional area that is displaced by the rods are given in Table 3.21. Note that this table gives displacement for a single rod in the bank, so the total displacement area

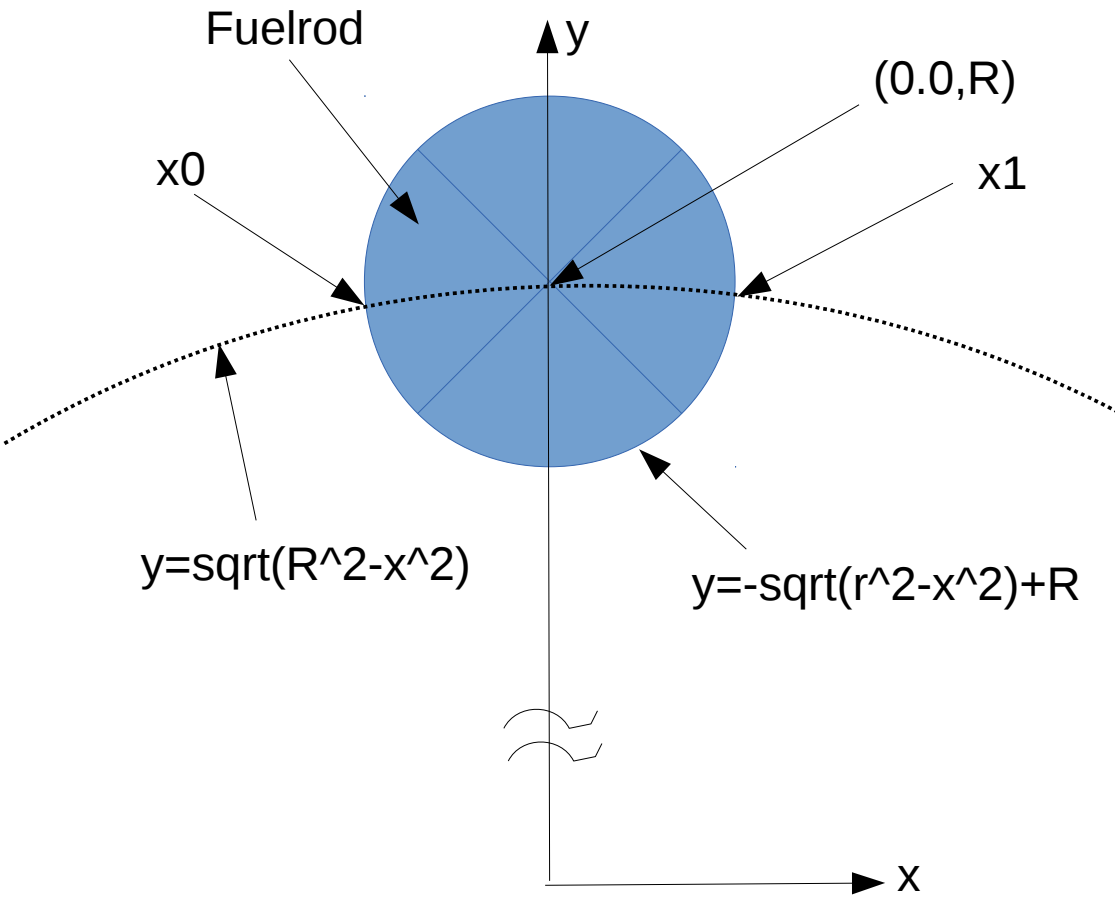

Figure 3.15: Defintion of functions for the circle that defines the fuelrod and the circle it sits on

Table 3.21: Channel area displaced by each rod bank

	Displacement of Channel Area (mm^2)				
Rod Bank	Ch 1	Ch 2	Ch 3	Ch 4	Num Rods
1	314.2	0.0	0.0	0.0	1
2	69.7	79.6	0.0	0.0	6
3	0.0	72.2	77.4	0.0	12
4	0.0	0.0	73.0	76.5	18

Table 3.22: Wetted perimeter of each rod in each channel of the model

	Rod Wetted Perimeter (mm)				
Rod Bank	Ch 1	Ch 2	Ch 3	Ch 4	Num Rods
1	62.8	0.0	0.0	0.0	1
2	19.5	23.9	0.0	0.0	6
3	0.0	20.5	22.8	0.0	12
4	0.0	0.0	20.9	22.4	18

of the entire bank must be calculated by multiplying the number of rods in the bank by the displacement of the single rod.

As a sanity check, it is prudent to compare the sum of the values in Table 3.21 times number of rods in the bank to a simple calculation of the total rod cross-sectional area in the test section. The rod cross-section area can be calculated simply as follows:

$$A = \frac{\pi}{4}20^2 + 36\frac{\pi}{4}13.8^2 = 5698.7\text{mm}^2 \tag{3.12}$$

Doing the math on Table 3.21 results in a total displacement area of 5696.2 mm^2, which agrees with our sanity check to within 0.04%, which can easily be accounted for by roundoff.

To figure out the wetted perimeter, it's necessary to find the angle between the two intersection points, x_0 and x_1, and the center of the fuel-rod circle. The trigonometric relation for determining this angle is presented below:

$$\theta = \pi - 2\cos^{-1}\frac{x_0}{r} \tag{3.13}$$

It's then possible to calculate the arc length between the two points with the relationship $\pi\theta$. The wetted perimeter of each rod in each ring is shown in Table 3.22. Similar to Table 3.21, the table gives wetted perimeter for a single rod in the bank (not the entire bank).

As a sanity check on the wetted perimeters, the total wetted perimeter of all rods is compared to the sum of the values given in Table 3.22 multiplied by the number of rods in each bank:

$$P_w = \pi 20 + 36\pi 13.8 = 1623.6\text{mm} \tag{3.14}$$

This compares favorable with the total displacement calculated from Table 3.22, which is 1622.2 mm. Note that in the CTF model, the wetted perimeter of the assembly casing is also added to Channel 4.

It is necessary to determine the azimuthal fraction of each rod bank in the channel so that rod heat is properly distributed into the channels. This can be obtained by taking the ratio of rod perimeter in the channel (given in Table 3.22) to total rod perimeter (43.4 mm). Azimuthal fractions of rods in given channels are shown in Table 3.23.

Table 3.23: Azimuthal fraction of each rod in each channel of the model

	Azimuthal fraction			
Rod Bank	Ch 1	Ch 2	Ch 3	Ch 4
1	1.0000	0.0000	0.0000	0.0000
2	0.4489	0.5511	0.0000	0.0000
3	0.0000	0.4736	0.5264	0.0000
4	0.0000	0.0000	0.4823	0.5177

Finally, the gap length and width must be determined to create the 3 gaps that exist between the 4 channels. The width is simply 7.8 mm, which was given in the facility schematic. The length is calculated as the distance between ring centers:

$$L = \frac{R_i - R_{i-1}}{2} + \frac{R_{i+1} - R_i}{2} \tag{3.15}$$

3.7.1.2 Axial Meshing

A schematic of the assembly in the axial direction is given in Figure 3.16. The figure shows the location of pressure taps with a "P" (e.g. P10, P11), thermocouples with a "T", and gamma densitometers (void measurements) with a "G". Spacer grid locations are labeled "Spacer" in the figure. The CTF model was made to cover the test section from the beginning of heated length (labeled as 0 in the figure) to the location of the P20 pressure tap, located at 4781 mm. As indicated in the drawing, the heated length is 4378 mm. The mesh cell sizing was meticulously set so that scalar cell centers lined up perfectly with the location of a pressure tap, thermocouple measurement, or gamma densitometer measurement. The scalar cell boundaries lined up perfectly with the location of spacer grids (which are placed at the center of momentum mesh cells in CTF). This ensured we could do direct CTF-to-experimental comparisons after running the simulation. A total of 123 mesh cells were used, leading to an average mesh cell height of 38.9 mm.

3.7.1.3 Boundary Conditions

Results were to be compared to those presented in Figure 26 of the test report[6], so the boundary conditions of the case presented in that figure were used. The boundary conditions were given in the table in Appendix 1 of the report. The inlet mass flux was 1026 kg/m^{2}s, the outlet pressure was set to 50 bar, and the inlet enthalpy was set to 1122.5 kJ/kg in order to achieve the specified inlet subcooling of 4.4 °C. The total test section power was 3000 kW, distributed uniformly throughout the test section. This test was a natural convection case.

3.7.1.4 Modeling Choices

Other important modeling choices included the selection of the grid loss coefficients and turbulent-mixing/void-drift parameters. Page 26 of the report specifies that the mean spacer grid loss coef-

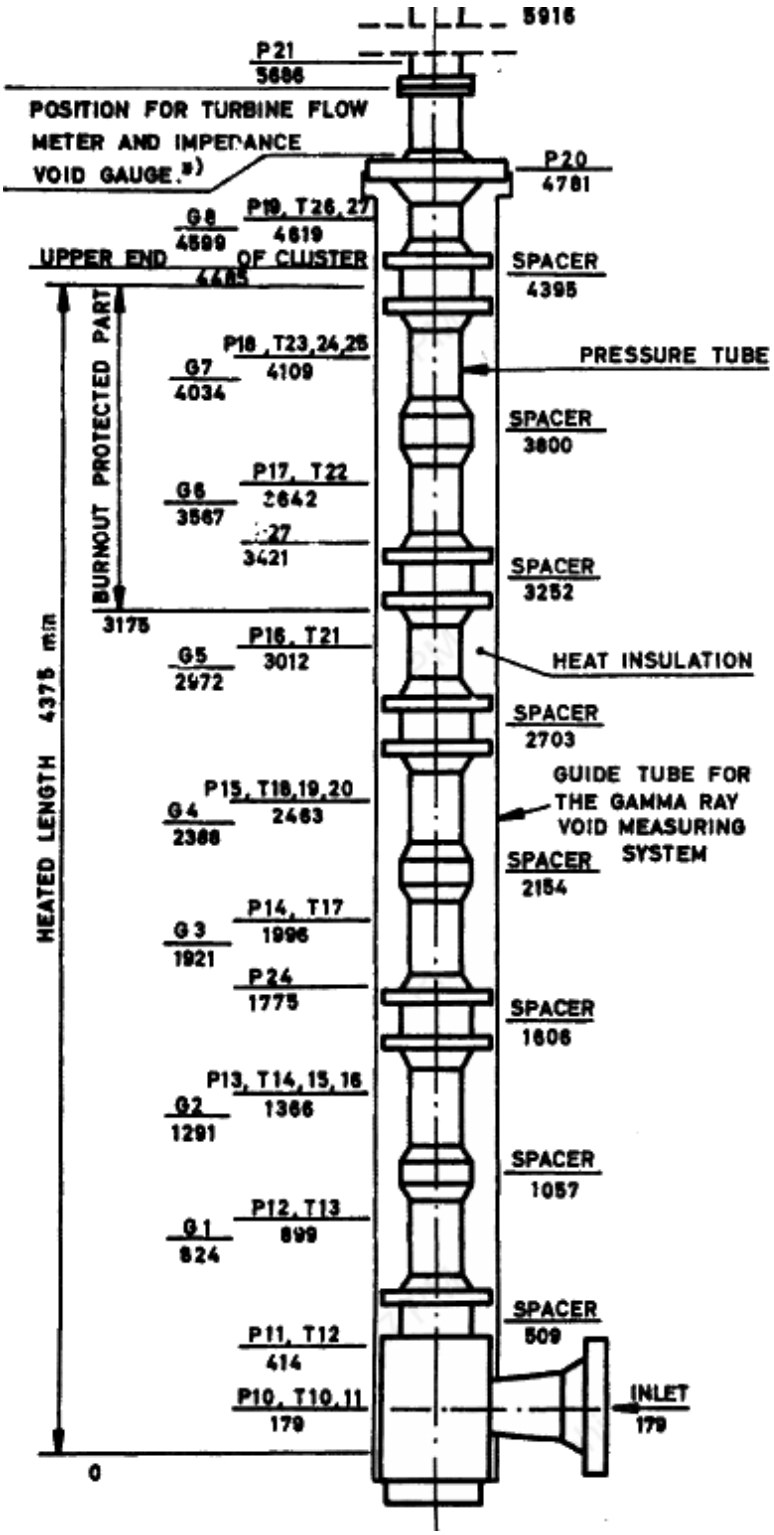

Figure 3.16: Schematic of FRIGG facility in axial direction

ficient was 0.58 for a Reynolds number of 2×10^5, so this value was used in the CTF model. The report also mentioned that the friction factor correlation for the test section was $f = 0.2Re^{-0.2}$. The friction correlation used in CTF is $f = 0.204Re^{-0.2}$, so it matches the one specified in the experimental documentation well. The mixing model was set to use Rogers&Rosehart to determine the single-phase mixing coefficient and Beus to determine the two-phase multiplier. The equilibrium void distribution weighting factor was set to the suggested value of 1.4 and the θ_M value was set to 5.0.

CHAPTER 4

EFFECTS TESTING

4.1 Comparison Metrics

In the following analysis, it is necessary to choose some metrics for comparing the accuracy of CTF in predicting the numerous QOIs. Most of this analysis is rather standard and simple, but for the sake of being clear and concise, some definitions are provided here.

We employ simple averaging to calculate average predicted and measured absolute values and, at times, also the average difference between measured and predicted values. This will be referred to as the "mean" or referenced symbolically as μ and is calculated as in Equation 4.1. In the equation, N is the number of values in the sample and x_i is the sampled value.

$$\mu = \Sigma_{i=1}^{N} \left(\frac{x_i}{N} \right) \tag{4.1}$$

The standard deviation, is in reference to the spread of the data that was averaged using Equation 4.1. It is calculated as shown in Equation 4.2.

$$\sigma = \sqrt{\Sigma_{i=1}^{N} \left(\frac{(x_i - \mu)^2}{N} \right)} \tag{4.2}$$

In order to make direct comparisons between the measured and predicted values, the Root-mean-square error (RMSE) is used, which is shown in Equation 4.3. It is a common metric for comparing predicted and measured values and is similar to the standard deviation, except that it compares the distances of the predictions from measured values. In the equation, x_{ctf} is the predicted value and x_{m} is the corresponding measured value. A note about this formulation is that it will exaggerate large differences between predictions and measured data due to the

squaring of the difference. Outliers are removed where appropriate, but this is clearly noted in the text when done.

$$\text{RMSE} = \sqrt{\frac{1}{N}\Sigma_{i=1}^{N}(x_{\text{ctf},i} - x_{\text{m},i})^2} \tag{4.3}$$

Both the standard deviation and RMSE will retain the units of the sampled value. This can be problematic when we want to compare data sets that were sampled from different operating conditions; in such a case, we expect the magnitude of the differences between measured and predicted results to change, so what we really want is to quantify the average of the relative differences. This is accomplished by taking the relative root-mean-square (rRMS) of the relative errors between measured and computed data. The relative error is defined as shown in Equation 4.4. The rRMS of the relative errors is defined as shown in Equation 4.5.

$$E_{\text{rel}} = \frac{x_{\text{measured}} - x_{\text{predicted}}}{x_{\text{measured}}} \tag{4.4}$$

$$\text{rRMS} = \sqrt{\frac{1}{N}\Sigma_{i=1}^{N}E_{\text{rel},i}^2} \tag{4.5}$$

4.2 Pressure drop

4.2.1 Pressure Drop in CTF

Prior to discussing results, a discussion of CTF-calculated pressure drop is in line. Some of the experimental results present only a component of pressure drop (e.g. frictional and acceleration pressure drop, having the gravitational component subtracted off of measured results during experimentation). CTF only solves for a single, total pressure in the model, but will still print out the pressure drop components (gravitational, frictional, and acceleration) to an output file by calculating the individual components of pressure drop upon completion of the simulation. Considering this, it is prudent to discuss the calculation of these terms prior to their use.

The acceleration pressure drop is calculated as the change in the momentum flux across a scalar mesh cell in the code.

$$\Delta P_{\text{accel}} = \left(\frac{G_m^2}{\rho_m^+}\right)_{\text{out}} - \left(\frac{G_m^2}{\rho_m^+}\right)_{\text{in}} \tag{4.6}$$

The momentum flux term is calculated as:

$$\frac{G_m^2}{\rho_m^+} = \rho_v \alpha_v v_v^2 + \rho_l \alpha_l v_l^2 + \rho_l \alpha_d v_d^2 \tag{4.7}$$

Here, α is the phase volume fraction, v is the phase velocity, and ρ is the phase density. The subscripts, v, l, and d stand for vapor, liquid, and droplets, respectively. In CTF, the momentum flux is calculated at the boundary of each mesh cell. Therefore, by taking the difference between momentum fluxes at two adjacent axial locations, we obtain the acceleration pressure drop over that corresponding scalar mesh cell.

The gravitational pressure drop is calculated for the scalar mesh cell as follows:

$$\Delta P_{gravity} = \rho_{\text{mix}} g \Delta X \tag{4.8}$$

Here, ΔX is the axial length of the scalar cell, g is the acceleration due to gravity, and ρ_{mix} is the mixture density, which is calculated as follows:

$$\rho_{\text{mix}} = \rho_v \alpha_v + \rho_l (\alpha_l + \alpha_d) \tag{4.9}$$

Finally comes the frictional pressure drop. It is simply calculated by subtracting the gravitational and acceleration losses from the total pressure drop calculated by CTF.

$$\Delta P_{\text{friction}} = \Delta P_{\text{total}} - \Delta P_{\text{accel}} - \Delta P_{\text{gravity}} \tag{4.10}$$

A final note on the calculation of pressure drop terms; these results were averaged across the whole cross-section of the model for a given axial level using an area-weighting approach.

4.2.2 BFBT

The BFBT tests contained both single-phase and two-phase pressure drop experiments. Single phase pressure drop results obtained from Series 7 are presented first, followed by two-phase pressure drop results from Series 6.

Single-phase pressure drop The ratio of measured-to-predicted pressure drop for all measurement locations are plotted against test Reynolds number in Figure 4.1. Note that the specification presented these pressure drop results as frictional loss only; the gravitational loss between pressure taps was subtracted off of the total loss before reporting data. Since CTF gives total pressure drop, it was necessary to subtract the gravitational component from the total loss between pressure tap locations.

From these results, we can see that the lower Reynolds test cases are generally under-predicted by CTF. As Reynolds increases past 100,000, the data seems to cluster better around the measurements. To more quantitatively capture the discrepancies between measured and predicted pressure drops, two statistics are shown in Table 4.1: the RMSE and the rRMS for each pressure tap. In addition to giving a discrepancy for each individual pressure tap, a total discrepancy for all test data is given in the last row of the table.

Table 4.1: RMSE and rRMS for measured and predicted data of BFBT P7 single-phase pressure drops

Pressure Tap	RMSE (kPa)	rRMS (%)
dp301	0.097	6.8
dp302	0.056	3.3
dp303	0.188	7.5
dp304	0.078	10.0
dp305	0.087	8.1
dp306	0.121	6.6
dp307	0.326	5.2
dp308	0.050	1.6
dp309	0.364	3.9
total	0.188	6.4

The RMSE metric is actually somewhat misleading because the collection of measurements taken at a given pressure tap were taken over a range of operating conditions. As the mass flow rate in the system increases, the pressure drop over a given tap increases as well, and with increasing pressure drop, we obtain increasing measurement error. Likewise, we expect more discrepancy between measured and predicted values as pressure drop increases. Therefore, it is not entirely fair to compare the RMSE of one pressure tap to that of another, as dp309, for example, which covers most of the test section, will have a much higher total pressure drop than dp301, which covers only 1 grid span. Inspection of Figure 4.1 clearly shows that the relative discrepancy between measured and predicted results for dp309 are slightly less than the relative discrepancy between measured and predicted results for dp301, actually. However, the RMSE in Table 4.1 would indicate otherwise, showing a discrepancy that is over 3 times higher for dp309.

This rRMS puts things into perspective by generating the average relative error for each pressure tap. We see that the average relative error of dp309 is only 3.9 %, which is better than dp301 discrepancy of 6.8 % as we expect. We also see that the pressure taps with the largest sources of error are dp303 and dp306. From Figure 4.1, we see that, in the case of dp303, CTF is over-predicting results and, in the case of dp306, CTF is under-predicting results. It is peculiar that this is the case, because the spans covered by these two pressure taps are about the same size (dp303 span is 466 mm and dp306 span is 512 mm). Additionally, both spans contain one grid. The experimental uncertainty for pressure drop given in the specification was 1%; the total rRMS value of Table 4.1 of 5% is far outside of this range.

Two-phase pressure drop The ratio of measured-to-predicted pressure drop is shown in Figure 4.2 with respect to bundle-averaged exit quality. The higher disagreement of Pressure taps 1, 2, and 3 become very evident in this figure and it seems there is very little correlation between the discrepancy and test quality.

Table 4.2 shows the RMSE and rRMS of the pressure drop differences grouped by pressure tap. The last row of the tables presents the statistics for the entire data set taken from all pressure taps and all test cases. From Table 4.2, we see that the first three pressure taps deviate most severely from the measured results. These particular spans are at the top of the bundle where void would be highest. For other spans, the rRMS is much more reasonable at around 5%. The total bundle pressure drops match experimental results (dp309) to within an rRMS of 2.9%,

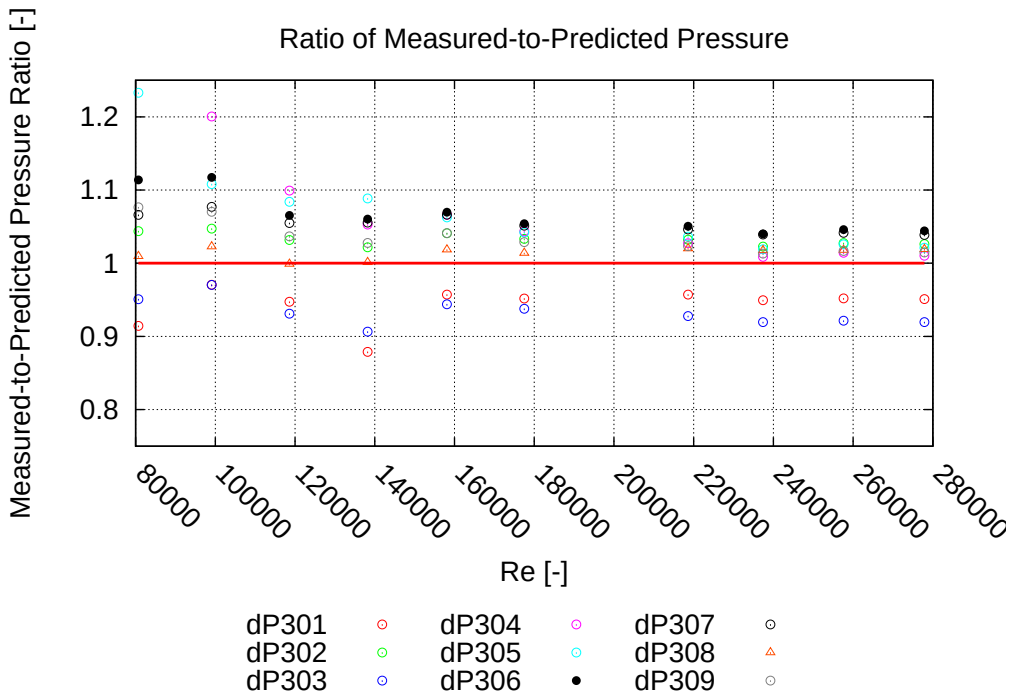

Figure 4.1: BFBT single-phase pressure drop predictions (Series 7)

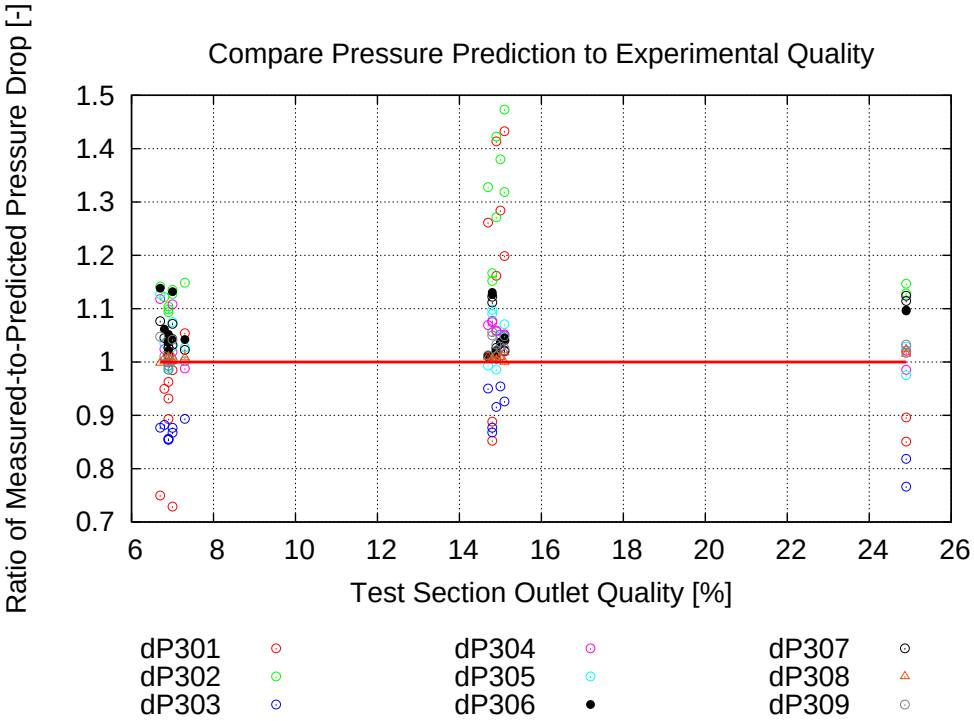

Figure 4.2: Ratio of measured-to-predicted pressure drop compared to bundle-average exit quality for BFBT two-phase tests (Series P6)

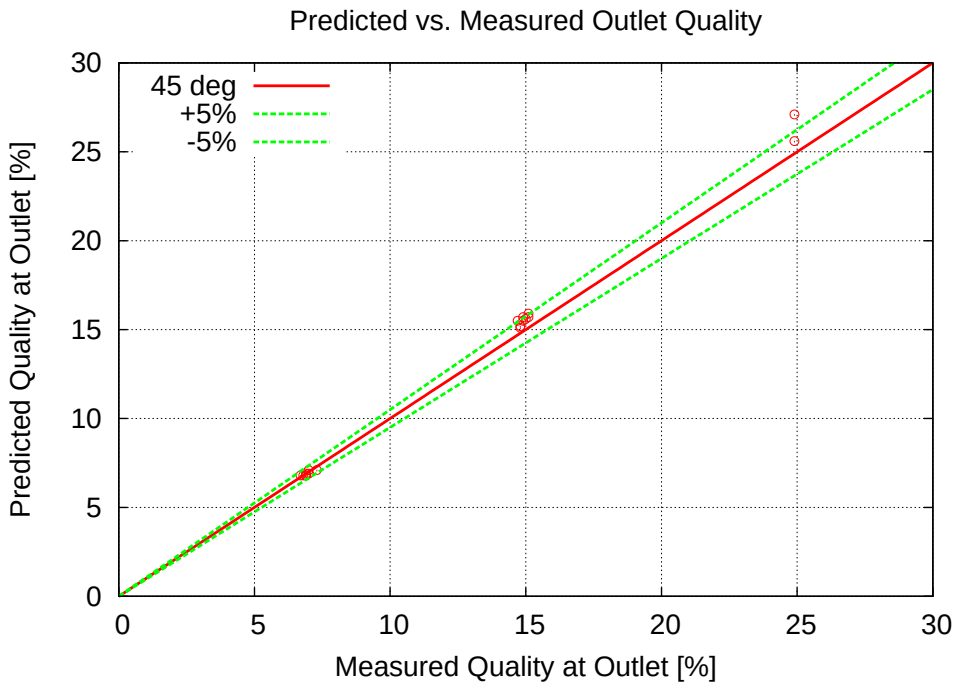

Figure 4.3: Comparison of measured and predicted bundle-averaged exit quality for BFBT P6 Series

which is very close to the rRMS obtained for dp309 in the single phase tests. Taking all data points into consideration leads to an rRMS of 11.0%. Like for the single-phase cases, experimental uncertainty was quoted to be 1%. The total bundle pressure drop matches experimental results fairly closely; it's the top span locations that lead to the large deviations from experimental results.

The average bundle-exit quality was also measured in the experiments. This result was also compared to CTF predictions. A figure comparing the measured to predicted values for the modeled tests is shown in Figure 4.3. Dashed lines are provided in the figure to act as a guide-post of sorts, showing where ±5% lies in the figure; the experimental uncertainty of the exit quality was not explicitly stated in the specification. The RMSE for the exit quality for all tests was 0.730 % (note, this represents an average variation of 0.00730 in predicted exit quality from measured exit quality, indicating close agreement in predicted and measured results).

Table 4.2: RMSE and rRMS of predicted and measured data of BFBT P6 Series two-phase pressure-drop measurements

Pressure Tap	RMSE (kPa)	rRMS (%)
dp301	1.596	19.3
dp302	8.550	18.4
dp303	0.920	15.0
dp304	0.295	3.5
dp305	0.336	4.1
dp306	0.365	6.4
dp307	0.740	5.2
dp308	0.465	6.4
dp309	1.676	2.9
total	1.123	11.0

4.2.3 FRIGG Facility

Cumulative pressure drop was actually broken up into three components in the experiment report: acceleration pressure drop, friction pressure drop, and gravitational pressure drop.

The comparison of the three pressure drop terms are shown in Figure 4.4. It's useful to note that pressure is shown in a cumulative fashion. In other words, the acceleration pressure drop profile includes both acceleration *and* gravitational pressure drop. Further, the friction pressure drop includes the effects of all three components. So, in reality, what is shown as the friction pressure drop is also the total pressure drop of the system. As this figure shows, CTF was able to match both the magnitude and behavior of each of the three components, in addition to the overall pressure drop of the system.

It should be noted, however, that the quantities used to plot experimental pressure drops were obtained from the original report using a digitizer which will contain a certain level of unknown error. Furthermore, the authors of the specification were not clear about how the components of the total pressure drop were calculated. Because of these factors, only the total pressure drop was considered in performing quantitative analysis. Taking the rRMS of the relative errors leads to an average difference of 6.3% per sampled data point.

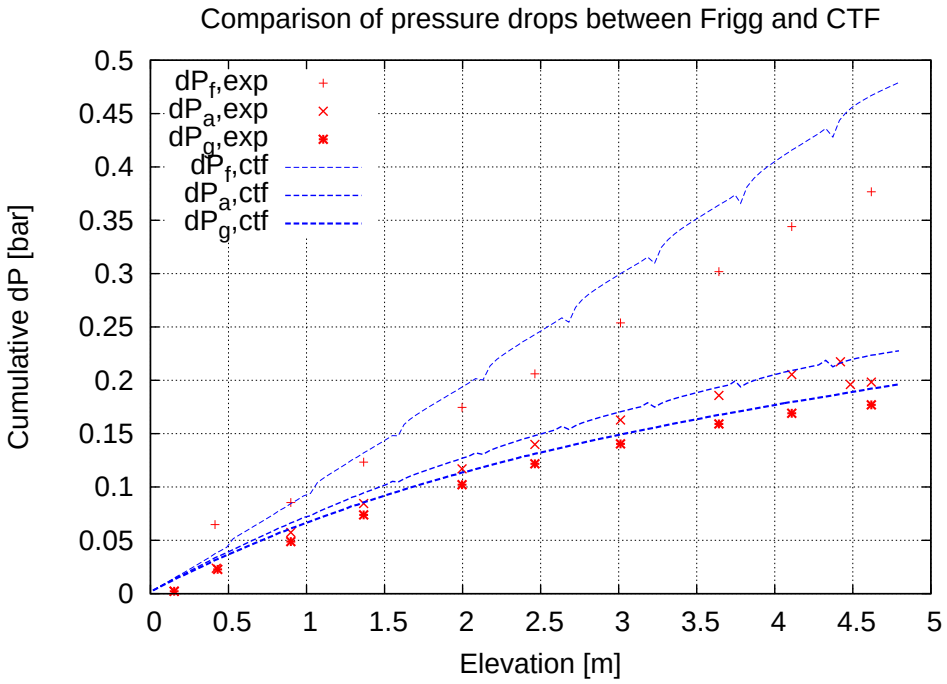

Figure 4.4: Comparison of experimental and predicted components of pressure drop

4.3 Void Content

4.3.1 PSBT

Void measurements were taken at three axial locations in the rod-bundle facility. The measurements represent the average void of the four subchannels surrounding the central rod. Table 2.4.1 of the specification[1] states that the rod-bundle void measurement uncertainty is 4%. To demonstrate CTF's capability to predict the void content in the flow, the predicted void (y-axis) is compared to measured void (x-axis) for the three test series. Results are shown in Figures 4.5, 4.6, and 4.7. In these figures, data that lands on the solid red line is in perfect agreement with the experimental results. The dashed green lines depict the experimental 2σ uncertainty of 4%. Data that falls within these dashed green boundaries are in agreement with experimental results to within experimental uncertainty.

The RMSE is provided for the three experimental series in Table 4.3. The statistics are provided for each test and each measurement location. Also, a summary of the statistics for all data in the series are given in the last row of the table.

Looking at the results of Table 4.3, there is no noticeable trend in error with respect to either test series or measurement location. In fact, the total test errors for each series are all pretty similar. We find that the RMSE comes out to about 0.053 for the entire group of tests, which sits just outside the experimental uncertainty of 4%. Considering that the RMSE calculation will magnify the larger errors, this is a very close agreement with experimental results.

The PSBT tests will exercise the inter-phase-mass-transfer (evaporation/condensation) and boiling models in CTF. Because the CTF predicted void around the center rod is being compared to measurements taken at the same location (as opposed to a bundle-average void), these tests will also exercise the void-drift model in CTF.

4.3.2 FRIGG Facility

The CTF prediction of the bundle-averaged void profile in the FRIGG facility is shown in Figure 4.8. The RMSE was calculated from all of the points that were sampled from the experimental results (summarized in Table 4.4). The RMSE is 0.0336, showing close agreement with experimental results.

Table 4.3: RMSE of measured and predicted void for PSBT Series 5, 6, and 7

Location	Series 5	Series 6	Series 7
lower	0.036	0.065	0.032
mid	0.045	0.046	0.072
upper	0.069	0.057	0.041
total	0.052	0.056	0.051

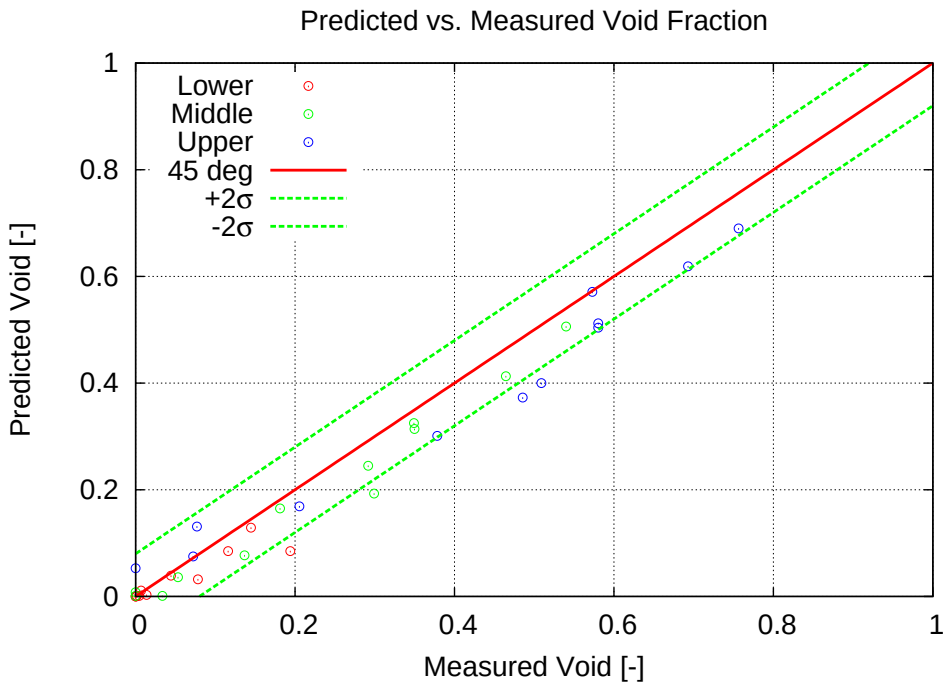

Figure 4.5: PSBT Series 5 predicted versus measured void around central rod in bundle

Table 4.4: Summary of void fractions sampled from FRIGG data report

Axial Location (m)	Measured Void (—)
0.824	0.252
1.291	0.304
1.921	0.469
2.388	0.618
2.972	0.607
3.567	0.676
4.034	0.696

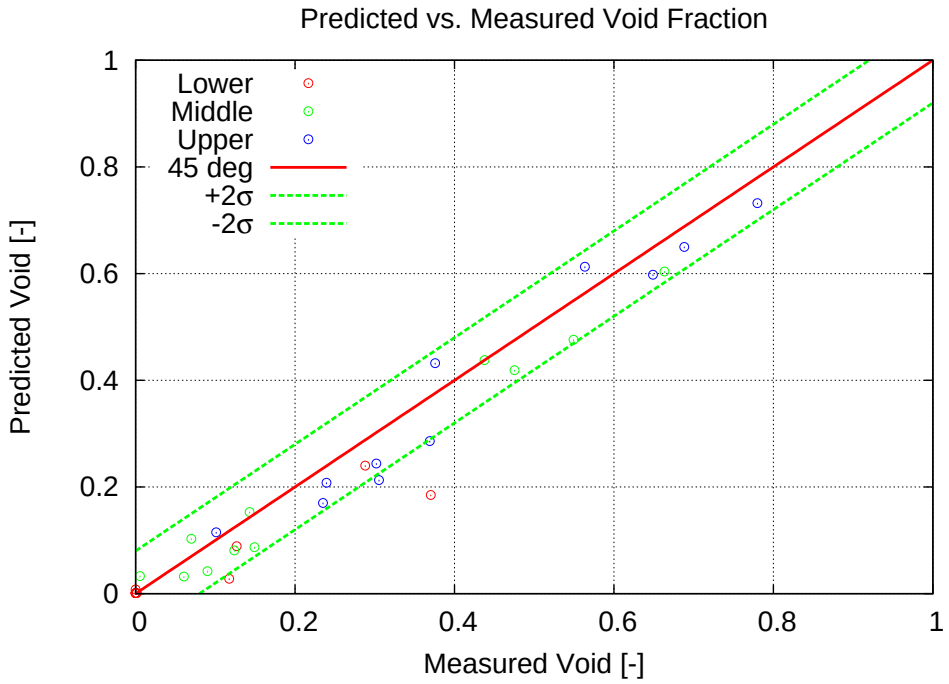

Figure 4.6: PSBT Series 6 predicted versus measured void around central rod in bundle

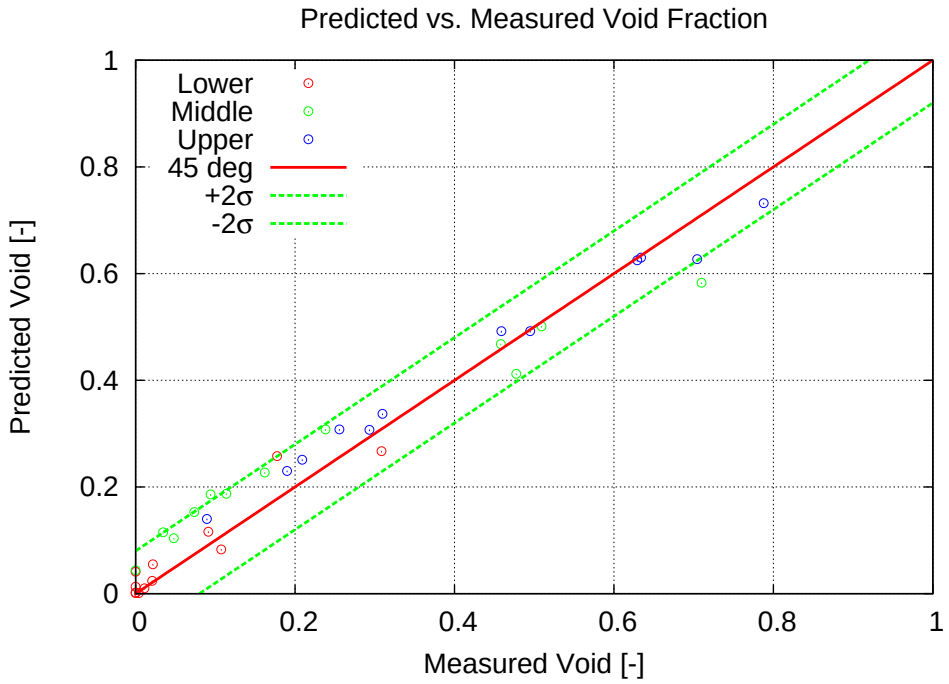

Figure 4.7: PSBT Series 7 predicted versus measured void around central rod in bundle

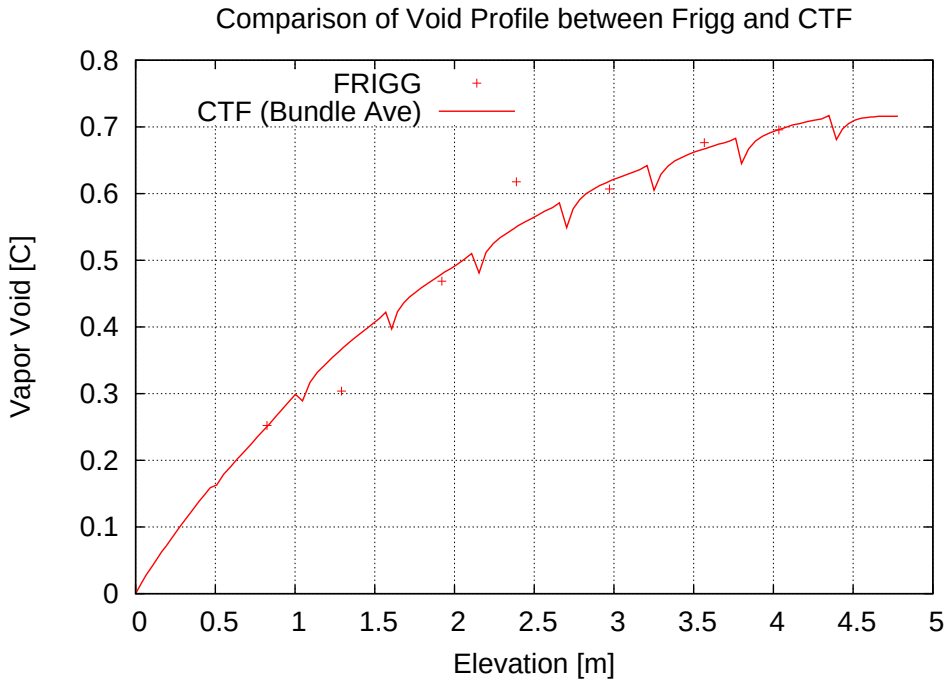

Figure 4.8: Predicted and measured axial bundle-averaged void profile in FRIGG facility

4.4 Departure from Nucleate Boiling

Prediction of Critical Heat Flux (CHF) in CTF primarily depends on the CHF model employed which, for these tests, was the "standard" model. This model considers three possible scenarios that can lead to CHF: pool-boiling, forced-convection boiling, and annular-film dryout. The means for selecting which scenario prevails is detailed in Section 4.4.2.1 of the CTF Theory Manual[9]. If in pool-boiling or annular film dryout, a modified-Zuber equation will be used. For forced convection, the Biasi equation is used. The critical heat flux (q''_{chf}) will be calculated at each timestep during the rod solution. The wall temperature required to make the nucleate boiling heat flux match the critical heat flux is calculated in an iterative fashion; this temperature is known as the CHF temperature (T_{chf}). When the actual wall temperature of the rod exceeds this T_{chf} value, a post-CHF heat transfer regime is entered and DNB occurs.

With this behavior, we can see that the CTF prediction of CHF will be affected by the CHF correlation employed and the heat transfer correlations employed (both single-phase convection and boiling).

4.4.1 Harwell Facility

The QOI for these tests is the location where dryout occurs. The experimenters reported the tube surface temperatures recorded by thermocouples attached to the outside of the test tube at discrete axial locations. A steep increase in temperature at a given thermocouple indicates a drop in heat transfer due to vapor blanketing of the tube surface (CHF). This location was selected in a subjective way by choosing the thermocouple reporting a steep temperature increase. Though, as evidenced by Figure 4.9, which shows the axial temperature distribution for one of the CHF tests and CTF predicted values, the point of dryout was typically very obvious.

Similarly, dryout was determined in CTF by looking at the tube surface temperatures reported in the results output file. A significant increase in temperature indicates a change in the heat transfer regime. Conveniently, the CTF output file also prints the heat transfer regime; a nucleate boiling heat transfer regime is pre-CHF and a transition boiling heat transfer regime is post-CHF.

A large set of test cases were modeled, 13 in total, in order to cover a wide range of operating conditions and generate good statistics. The predicted dryout location is plotted against the experimental observed dryout location in Figure 4.10. A note about the error bars on the data is in order for this figure. The experimental uncertainty comes from the fact that the thermocouples are placed at discrete locations. If a thermocouple reads an elevated temperature due to vapor blanketing, it does not necessarily mean that CHF occurred at exactly that axial location. Rather, CHF could have occurred at any axial location upstream of that thermocouple, up to the next thermocouple which is not reading an elevated temperature. The experimental uncertainty bars represent this distance to the next upstream thermocouple.

The error bars on the CTF predicted location represent the fact that CTF did not give a single location for CHF. Rather, for some test cases, the tube surface temperature shot up in one axial level, then dropped back down in the next axial level, then shot up in the level above that, and so on. Some test cases gave a single axial location where temperature increased, but others saw two or three oscillations in temperature with increasing height before the temperature became continuously elevated. In the event of such oscillations, the point where temperature

became continuously elevated was selected as the predicted dryout location. The error bars on the CTF predictions then wrap any oscillations in temperature that occur upstream of that location. From Figure 4.10, you can see that these oscillation regions were relatively small compared to experimental uncertainty. Furthermore, in no case did the these oscillations result in the CTF predictions falling in the range of experimental dryout location.

The discrepancy between calculated and measured dryout location is capture with the RMSE statistic. As stated before, the CTF dryout location is chosen as the axial location where the wall temperature becomes constantly elevated. The measured dryout location is set at the thermocouple where temperature is observed to rapidly increase, even though the actual dryout location may occur further upstream. Using all 13 data points leads to an RMSE of 0.478 m. From Figure 4.10, we can see that there are two outliers that will skew that statistic significantly. Leaving them out of the calculation leads to a discrepancy of 0.281 m.

It is also important to take note of the direction of the skewing, as predicting CHF to occur sooner than it actually does represents a conservative calculation, as CHF is a limiting term in safety analysis. We can see that the two outliers both show that CTF is predicting CHF to occur lower in the test section, or sooner, than it actually occurs. Calculating the average discrepancy for the non-outliers using Equation 4.11, leads to a discrepancy of -0.129 m. This is also a more conservative prediction, on average, of the CHF location.

$$E = \frac{1}{N}\Sigma_i(x_{\text{ctf}} - x_{\text{exp}}) \tag{4.11}$$

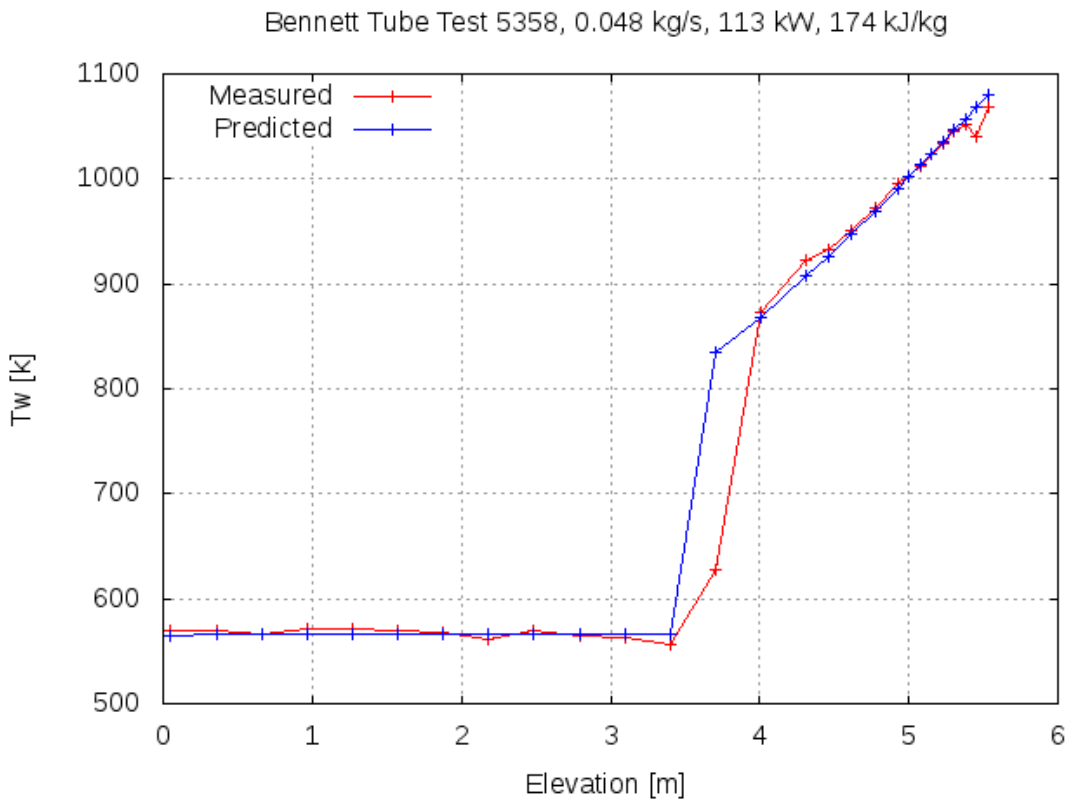

Figure 4.9: Comparison of predicted and experimental axial temperature profiles for Harwell Test 5358

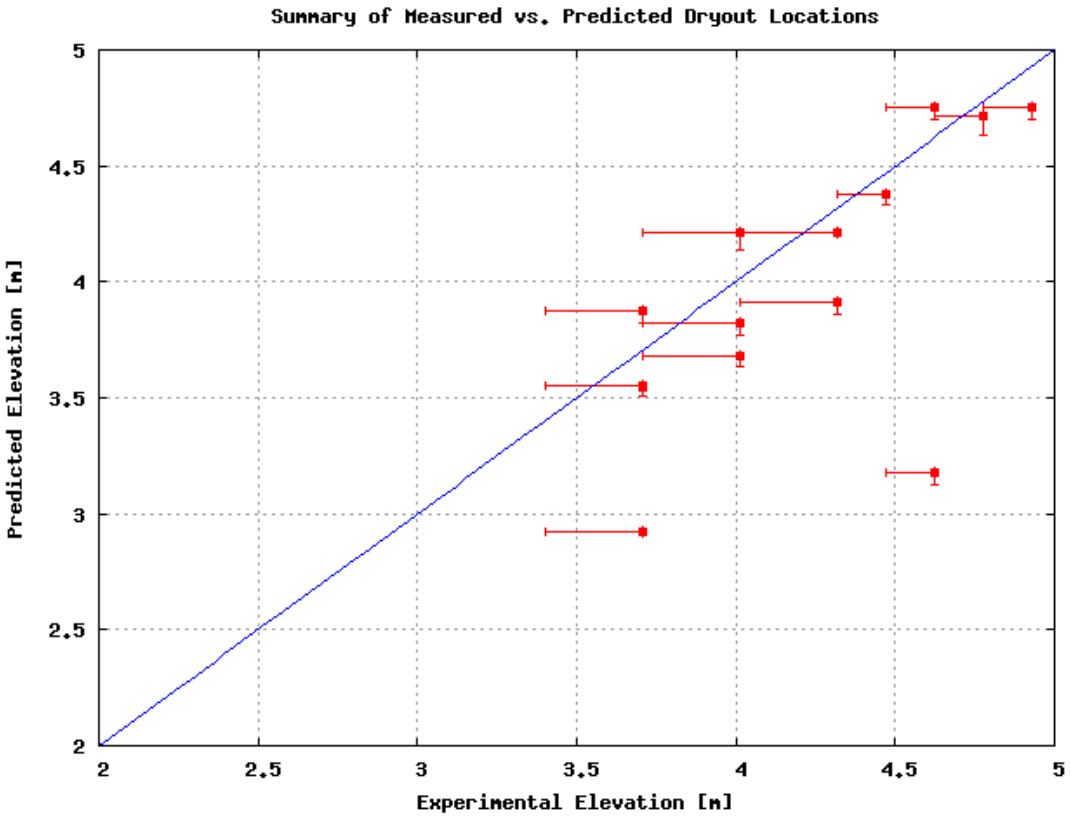

Figure 4.10: Summary of predicted and experimental dryout locations for Harwell test cases modeled by CTF

4.5 Turbulent Mixing & Void Drift

4.5.1 GE 3x3

In the GE 3x3 experiments, the experimenters were able to measure individual subchannel exit equilibrium quality and mass flux. By comparing CTF predictions of these quantities to experimental values, it allows us to gauge the effectiveness of the turbulent mixing model in the code. Since these tests include cases with large amounts of voiding, the impact of the void drift model can also be assessed. Of course, other effects will play into the void content and mass flux in individual subchannels, so this is not exclusively a test of the mixing and void drift model.

A comparison of the measured and predicted exit equilibrium qualities is provided in Figure 4.11. An extensive error quantification study was carried out by the experimenters to account for experimental measurement errors. The authors determined that the error in the exit equilibrium quality measurements were ± 0.02. The error in the mass flux measurements was $\pm 3\%$ and the error in the enthalpy measurements was also $\pm 3\%$[8].

Figure 4.11 demonstrates that most predicted exit qualities fall within experimental uncertainty. However, the values that seem to vary furthest from measured results are qualities in the corner type subchannel. Calculating the RMSE for the three subchannel types leads to the results in Table 4.5. We see that, on average, the corner channel quality predictions are more than 0.01 larger than the Inner and Side type channel predictions. Furthermore, from Figure 4.11, we see that quality in the corner channels is typically over-predicted by CTF.

In addition to the exit equilibrium quality, the authors also measured the exit mass flux of each individual subchannel type. This is presented in Figure 4.12. Additionally, the RMSE is given for each subchannel type to quantify the difference between predicted and measured values in Table 4.6. Since quality in corner channels demonstrated the greatest deviation from experimental results, we also expect the mass fluxes in the corner channels to deviate further from their experimental counterparts compared to side and inner types. The RMSE of the mass fluxes show that this is, indeed, the case with mass fluxes in corner type channels being off by about 80 kg/m^2-s from their experimental counterparts. The Inner type channel, by comparison, is off by about 38 kg/m^2-s from experimental data.

Since we look to assess the impact of the void drift model in this section, an additional set of cases was run with the void drift model shut off (note that turbulent mixing was still on). This leads to the following outlet quality and mass flux shown in Figures 4.13 and 4.14. It is clear that the results have gotten worse, mostly in the peripheral subchannel types. The RMSE statistics, shown in Tables 4.7 and 4.8 for these channels indicate the degree to which results have degraded.

Table 4.5: RMSE of exit equilibrium quality for GE 3x3 modeled tests

Channel Type	RMSE (-)
Corner	0.029
Side	0.016
Inner	0.015

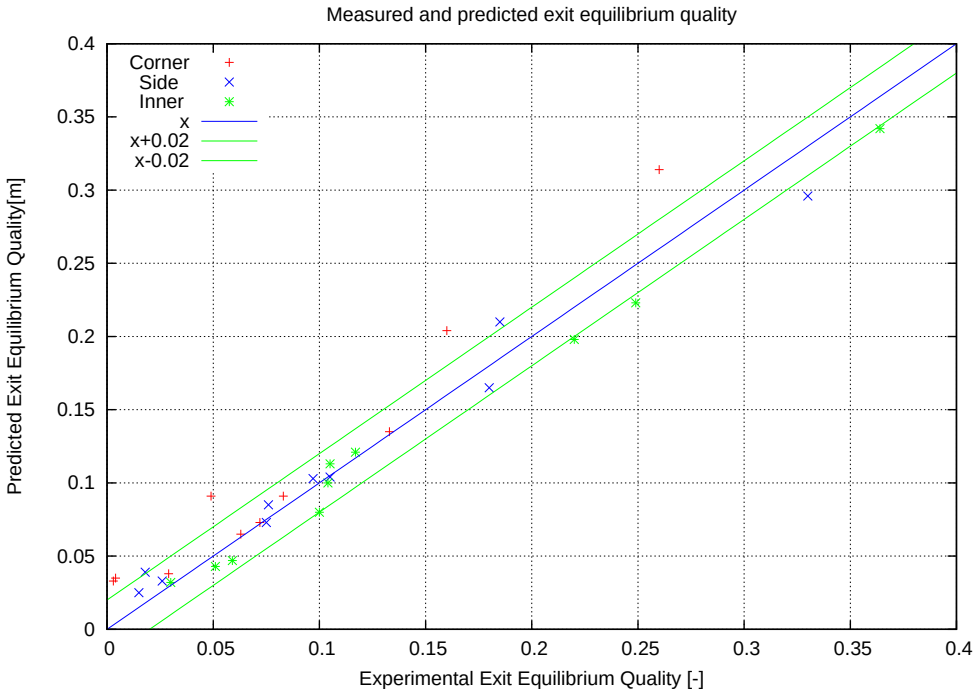

Figure 4.11: Measured vs. predicted exit equilibrium quality in individual subchannels of the GE 3×3 cases

Table 4.6: RMSE of exit mass flux for GE 3x3 modeled tests

Channel Type	RMSE (kg/m^2-s)
Corner	79.96
Side	31.22
Inner	38.03

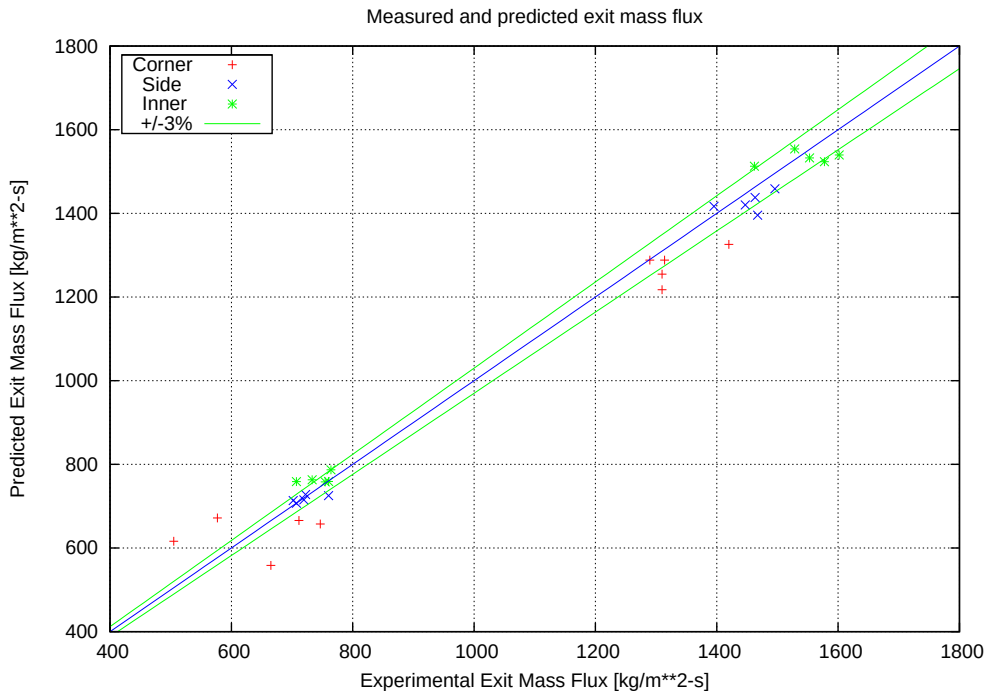

Figure 4.12: Measured vs. predicted exit mass flux in individual subchannels of the GE 3×3 cases

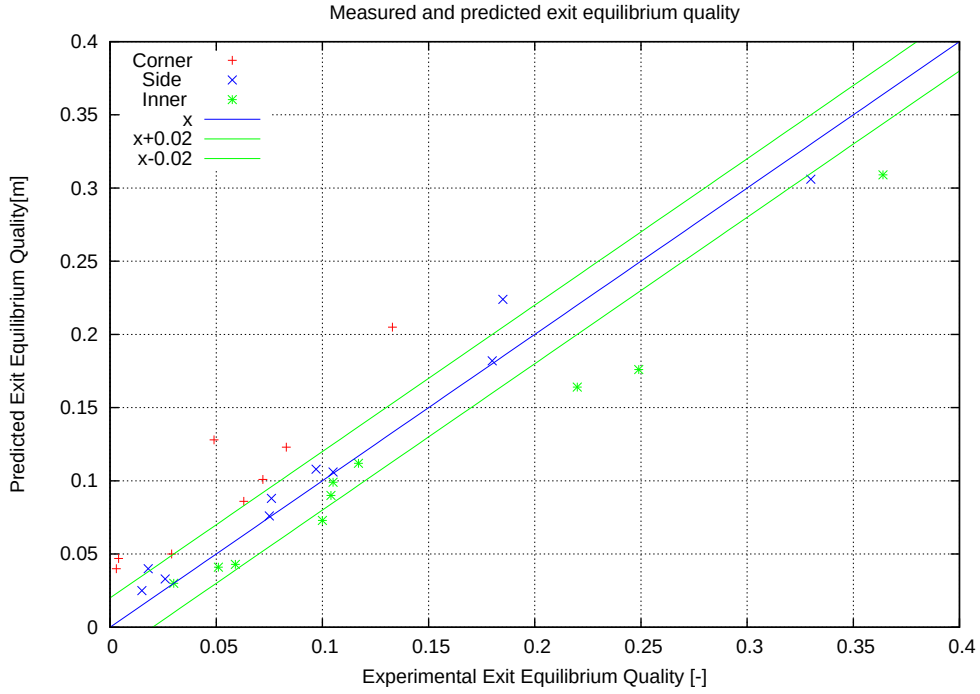

Figure 4.13: Measured vs. predicted exit equilibrium quality in individual subchannels of the GE 3×3 cases with void drift model turned off

The subchannel type that saw the most degradation in accuracy was the corner type. The RMSE for the corner channel exit quality jumped from 0.029 up to 0.134 after shutting off void drift; a change of 0.105. However, the inner channel exit quality RMSE went up by only 0.021 from 0.015 to 0.036. This indicates that the void drift model has the most significant impact on channels with the smallest flow area, but note that the inner channel quality error still doubled after shutting off the void drift model. The mass flux statistics show the same behavior, with corner channel RMSE jumping from 80 to 260 kg/m^2-s.

4.5.2 CE 5x5

The CE 5x5 tests were performed for the purpose of assessing heat transfer models. Test conditions were run such that all regions of the boiling curve were experienced from single-phase convection up to CHF. Temperature measurements were made on the rod surfaces via thermocouples attached to the inside of the heater tubes. However, it is also possible to assess coolant mixing between channels because thermocouples were also placed at the outlet of the test section in the center of each of the 36 coolant channels.

Table 4.7: RMSE of exit equilibrium quality for GE 3x3 modeled tests when void drift model is turned off

Channel Type	RMSE (-)
Corner	0.134
Side	0.017
Inner	0.036

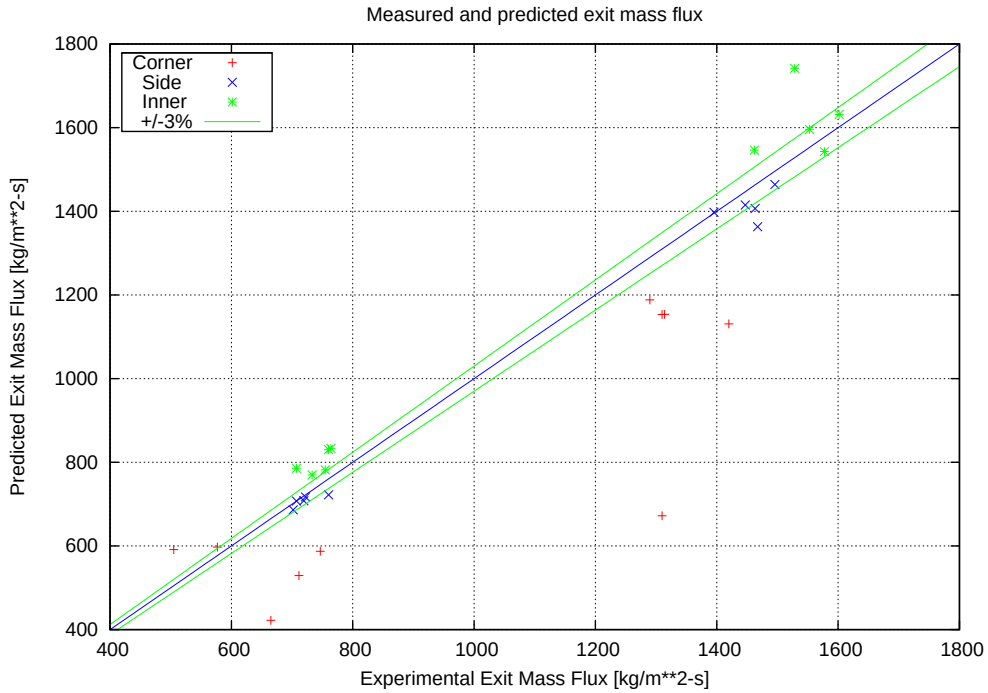

Figure 4.14: Measured vs. predicted exit mass flux in individual subchannels of the GE 3×3 cases with void drift model turned off

Table 4.8: RMSE of exit mass flux for GE 3x3 modeled tests when void drift model is turned off

Channel Type	RMSE (kg/m^2-s)
Corner	260.1
Side	42.32
Inner	86.27

Test 74 was simulated with CTF, which was actually a collection of over 70 separate experiments with different operating conditions that led to different heat transfer mechanisms. The primary operating condition that was modified was the test heat flux. Each individual test was simulated with CTF, then the predicted outlet temperature of each channel was compared to the measured outlet temperature for that channel in the bundle. This was done for all tests in the series and then a mean difference between predicted and measured values was obtained for each channel. A graphical representation of these mean differences are shown in Figure 4.15.

It is important to note that, prior to doing any data comparison on the outlet temperatures, *outlier data points were removed*. To demonstrate the existence of outliers, see Figure 4.17, which shows the measured and predicted outlet temperatures for Channel 36 of the test section over all test cases. You can see points for three low heat flux cases that are clearly outliers from the rest of the experimental data. To prevent such data from polluting the summary statistics, any data that led to a discrepancy of more than 50 F between predicted and measured results was eliminated from the analysis.

Returning to Figure 4.15, this plot is useful in demonstrating two things: first, the mean discrepancies fall between ± 10 F and, second, the largest errors seem to occur in the corner and side channels of the bundle. A more quantitative view of the data is presented in Figure 4.16. This figure shows a few important things. First, the data is organized by channel type: red dots represent the side-type channels, green dots represent the inner-type channels, and blue dots represent the corner type channels. Additionally, the data are plotted against channel index on the x-axis. The indexing scheme is such that channel numbers start at the north-west corner of the bundle and increase going west-to-east and north-to-south. What we see in this figure is similar to what we saw in Figure 4.15; the corner and side channel discrepancies are generally further from the experimental results than the inner-type channels.

Additionally, this plot also shows the mean discrepancy with the horizontal pink line; it is calculated as an average of all the channel mean discrepancies after removing the outlier discrepancies. We can see that, in general, CTF is over-predicting the experimental results by 2 F. This is what we would expect because the experimental temperature measurements are made in the center of the subchannel, whereas the CTF predictions are the temperature for the entire fluid control volume. The experimental thermocouple measurements will not capture the higher temperatures of the fluid right next to the rod surface, but the CTF predictions will, which acts to raise the average temperature in the control volume.

Finally, this plot also shows the 2σ variation in experimental temperature measurements for each thermocouple. Note, the error bars are *not* showing the standard deviation in the mean discrepancy that is shown. For example, for Channel 7, we see the discrepancy is about 0.5 F, but the error bars show that the experimental measurements varied by about 0.5 F during successive measurements taken in the calibration phase of the tests. So the actual discrepancy can be anywhere between 1.0 and 0.0 F for this thermocouple because we can only rely on the temperature obtained from the thermocouple to within 0.5 F.

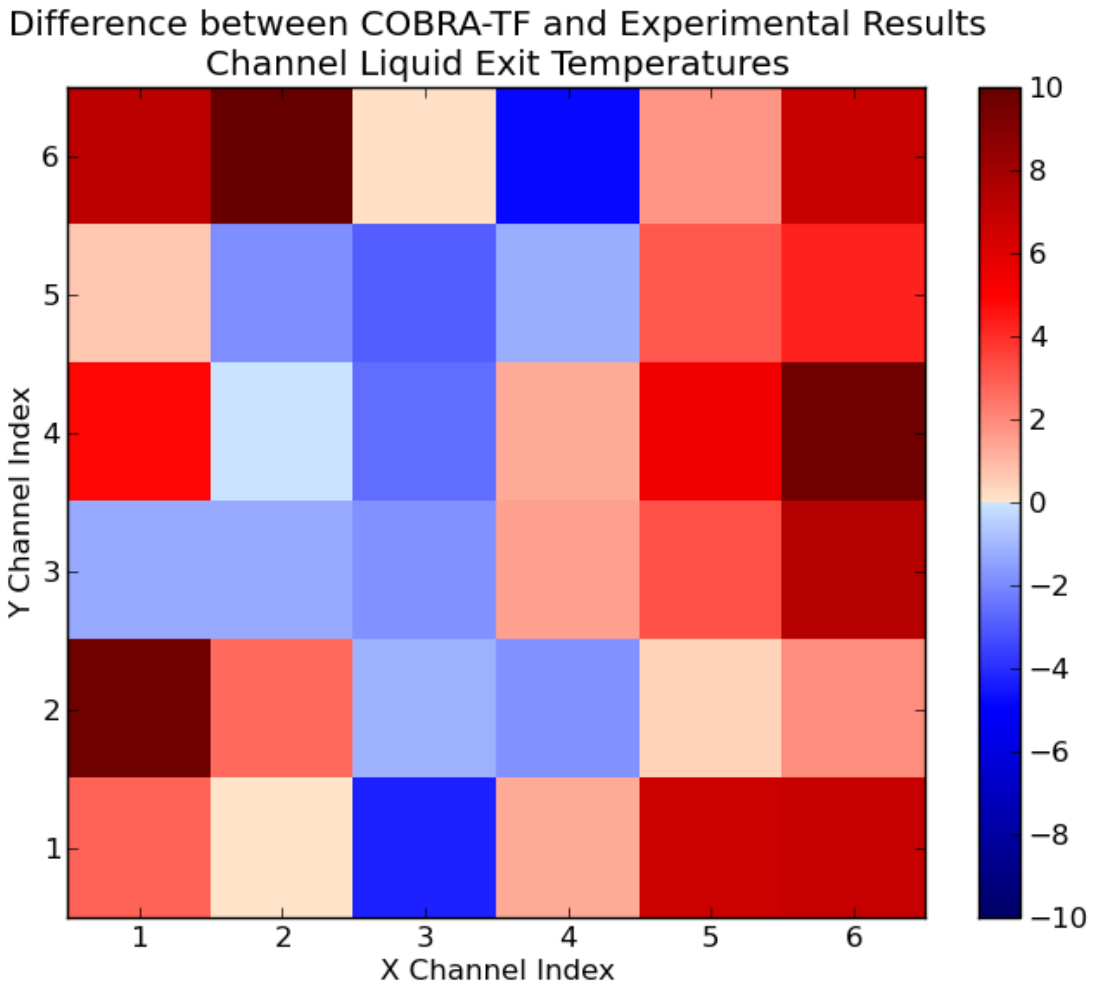

Figure 4.15: Average difference between CTF predicted channel exit temperatures and experimental values for all tests in CE 5x5 Series 74

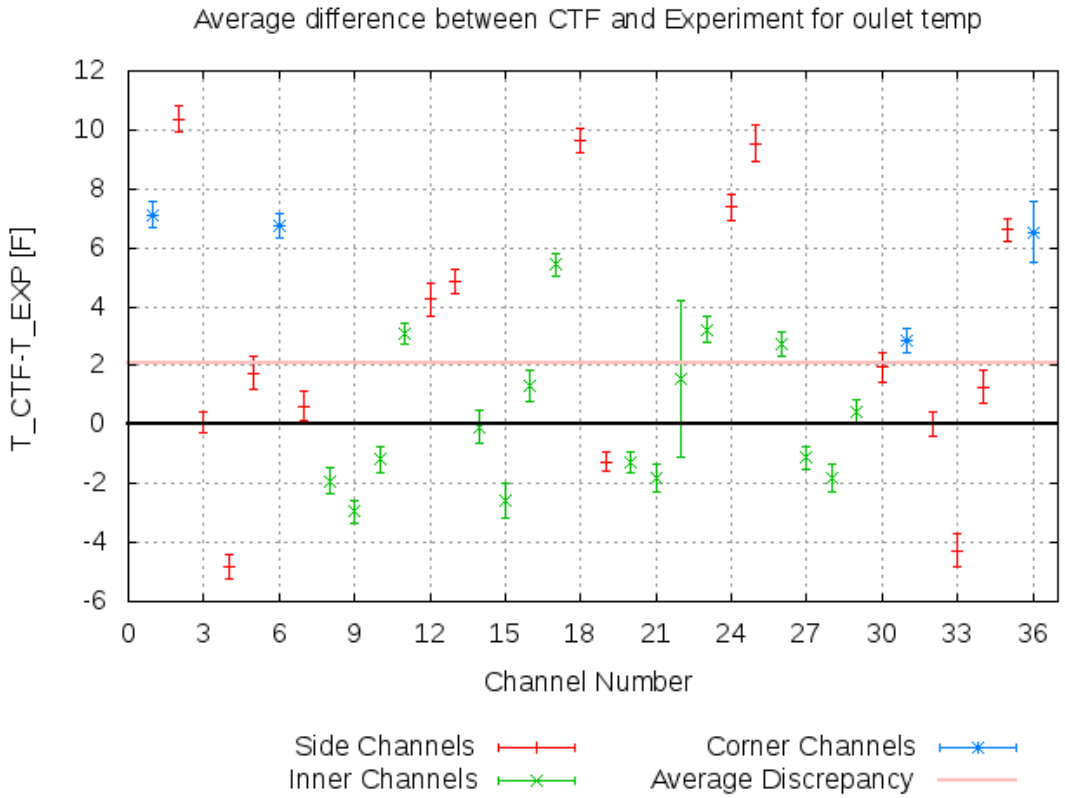

Figure 4.16: Average difference between CTF predicted channel exit temperatures and experimental values with measurement error and mean discrepancy

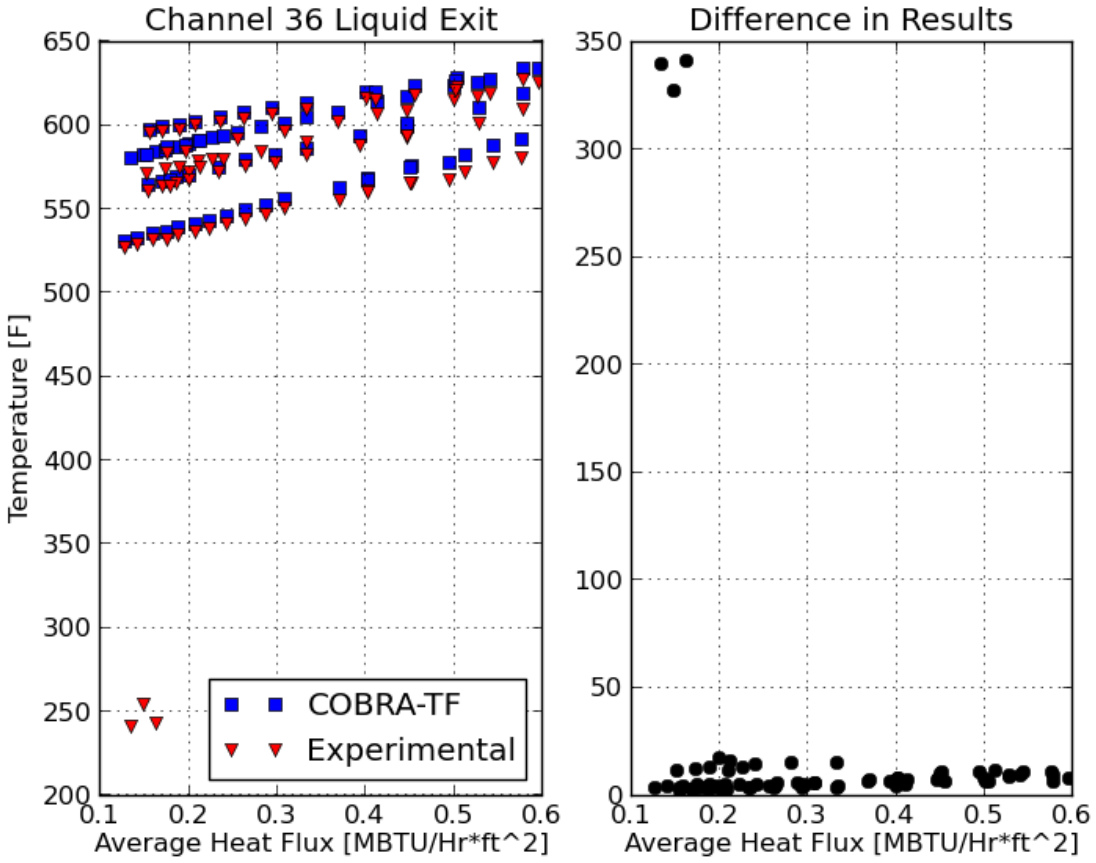

Figure 4.17: Predicted and measured outlet temperatures for Channel 36 in all CE 5x5 Series 74 cases

4.6 Heat Transfer

When discussing the heat transfer models in the code, what we really care about is the accuracy in the calculation of the Heat Transfer Coefficient (HTC), h, that is used in Newton's Law of cooling:

$$q'' = h\,(T_w - T_b) \tag{4.12}$$

where q'' is the heat flux from the wall to the fluid, T_w is the temperature of the wall surface, and T_b is the temperature of the bulk fluid (in the case of a subchannel code, this is the control volume temperature of the fluid).

It is not possible to calculate h directly in experiment but, rather, it must be back-calculated from the experimental measurements of T_w, T_b, and the known rod power of q''. Since there are difficulties in obtaining values of T_b from experiment for the rod-bundle geometry that we are concerned with (associated with holding a thermocouple in a given position of the flow channel and also its impact on the fluid behavior), T_b values are typically not available. The T_w measurements are much more easily available as the experimenter can insert a thermocouple in the inside of the heater tube, where there is no flow, fix it to the wall, and then post-process the data by solving the 1-D conduction equation for the tube thickness in order to yield the outer tube surface temperature.

In order to actually obtain the experimental value of h, this then leaves us with using the subchannel code to estimate values of T_b at the T_w measurement location so that we can solve Equation 4.12. Of course, this then begs the question of what is the validity of the estimates of T_b. Rather than introduce this uncertainty into the analysis, we instead directly compare CTF estimates of T_w to experimental results. Since the value of the measured wall temperature will be directly related to the magnitude of the convective and boiling heat transfer in the experiment, this is a suitable check on the effectiveness of the employed heat transfer models in CTF.

4.6.1 CE 5x5

The CE 5x5 tests involved running over 70 tests of varying operating conditions on a 5x5 electrically heated rod bundle facility. The operating conditions were varied such that heat transfer mechanisms in the bundle ranged from single-phase convection to saturated boiling. Instrumentation included thermocouples fixed to the interior of two of the heater rods.

In Rod 25, the central heater rod, 14 thermocouples were placed at 4 different levels: 76.63, 81.00, 82.50, and 83.50 inches from BOHL. One set of thermocouples sat below a mixing vane grid and the other three sets were above the grid. The set below the grid included two thermocouples placed at two different azimuthal locations. The three sets above the grid each included 4 thermocouples placed at 4 azimuthal locations. In Rod 24, the adjacent rod to the west of Rod 25, 4 thermocouples were placed. A single thermocouple was placed below the grid and two sets of thermocouples were placed at two levels above the grid.

Using the temperature for a given thermocouple over all the testing conditions clearly reveals the incipience of boiling at that position in the bundle with a leveling-off of the temperature

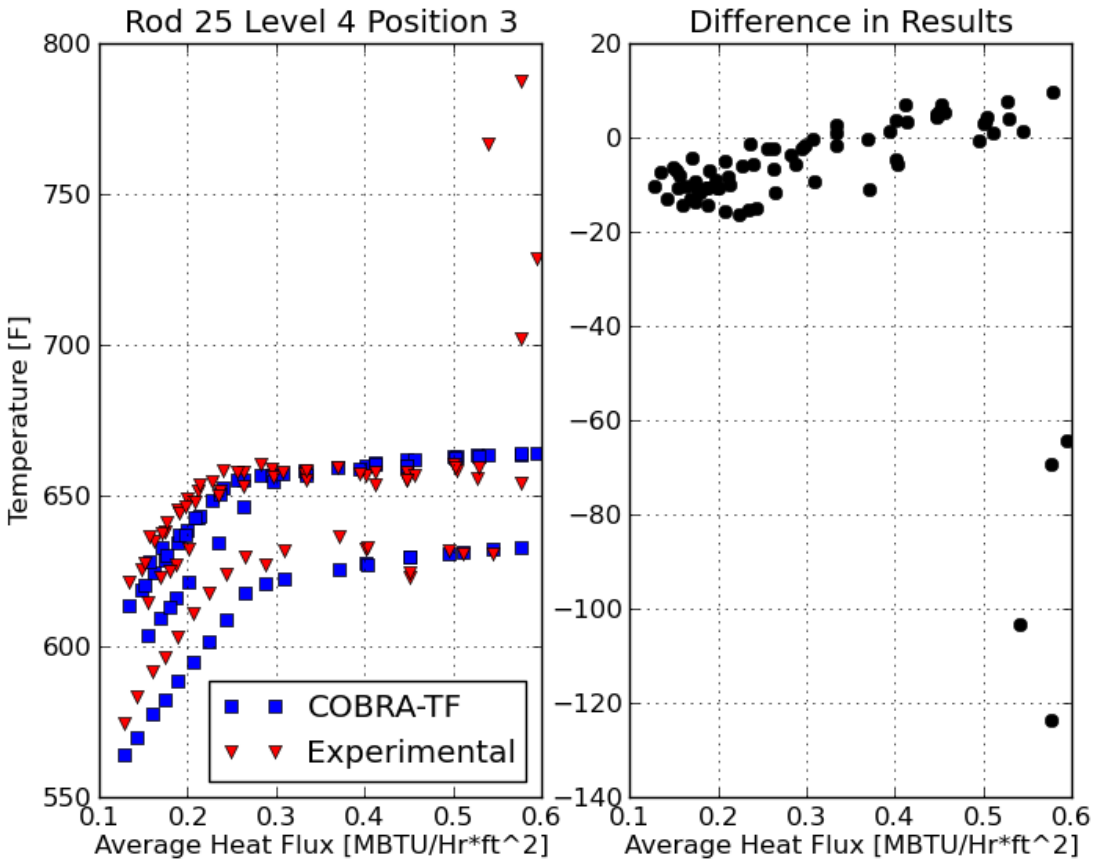

Figure 4.18: Rod surface measurements and predictions with respect to increasing test heat flux for Rod 25 (central rod) at 77.63 inch axial location

profile with respect to bundle heat flux. Figure 4.18 shows this axial profile along with the difference between CTF rod surface temperature predictions and the experimental results. This figure also shows another important thing, which is the existence of outliers in the data. Like for the exit channel temperatures, outliers were eliminated from the data set before doing any data analysis. Again, a discrepancy of greater than 50 F resulted in the data set being removed.

After eliminating outliers, some data reduction was done to generate a more meaningful overview of the predictive capabilities of CTF. First, the merit of interest is the difference between predicted and measured rod surface temperatures. Second, the mean of this discrepancy was calculated for each thermocouple for all tests that were run, leaving us with one mean discrepancy per thermocouple (20 in total). These discrepancies are presented in two figures—one figure for each of the two instrumented rods. Rod 25 results are given in Figure 4.19 and Rod 24 results are given in Figure 4.21.

In the figures, the x-axis shows the axial location of the thermocouple. The thermocouples, as placed in the figure, are not exactly accurate to their placement in experiment. The red thermocouple (Position 1) is placed at the actual location in the experiment. The following

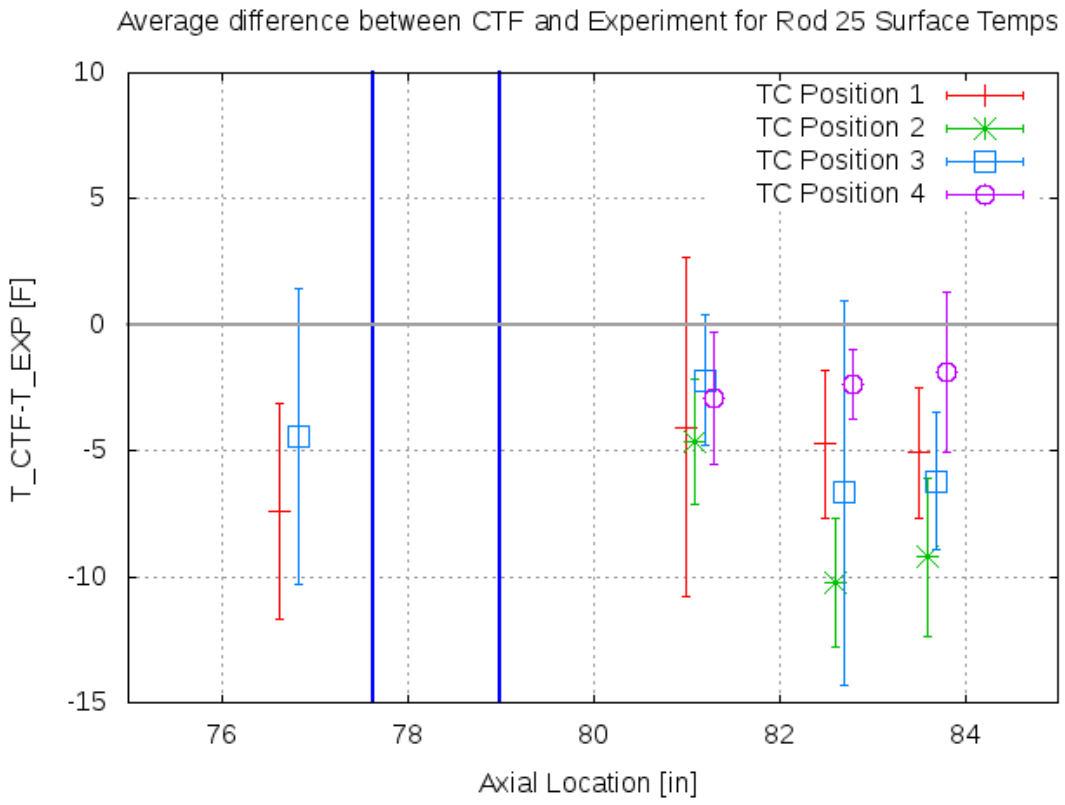

Figure 4.19: Summary of mean difference between predicted and measured rod surface temperatures for each thermocouple in Rod 25 over all test cases

three thermocouples are shifted over to the right slightly to aid in viewing the data. In reality, all thermocouples for a given axial location are at exactly the same axial position in the bundle. The y-axis is the difference between predicted and experimental rod surface temperatures. The two vertical blue lines represent the bottom and the top of the spacer grid. Finally, the error bars do not represent the scatter in the discrepancies for each mean discrepancy. Rather, they represent the 2σ scatter of the experimental measurements during the calibration phase of the experiment. For example, in Figure 4.19, the blue thermocouple before the grid has a scatter in measurements of over 5 F. The mean discrepancy between predicted and experimental data is about -5 F. Considering the scatter in the thermocouple readings, the actual discrepancy may be anywhere between -10 and 1 F.

From the results, we can see that Rod 25 rod temperature predictions are all lower than experimental results, which means that CTF is over-predicting the heat transfer from the rod. As a note, the grid enhancement model was not turned on for these experiments, which should cause an under-prediction in heat transfer downstream of the grid. Actually, we don't see any trend in the data before or after the grid in these results. We do see a significant degree of azimuthal variation in the rod surface temperatures (as high as 12 F at the 83.5 inch location), which we should expect given that the test section uses Mixing Vane Grid (MVG)s (see Figure

4.20). It is important to note that CTF has no mixing vane grid models to account for these types of effects. However, some of this scatter must also be related to uncertainty in the experimental measurements, as the level prior to the grid sees a 3 F azimuthal variation. Also, we see that, in many cases, the 2σ scatter in experimental measurements is enough to account for this azimuthal variation.

Overall, for Rod 25, the mean difference between CTF predictions and measured wall temperatures is -5.14 F. For Rod 24, the under-prediction of wall temperature is less severe, averaging out to -1.71 F.

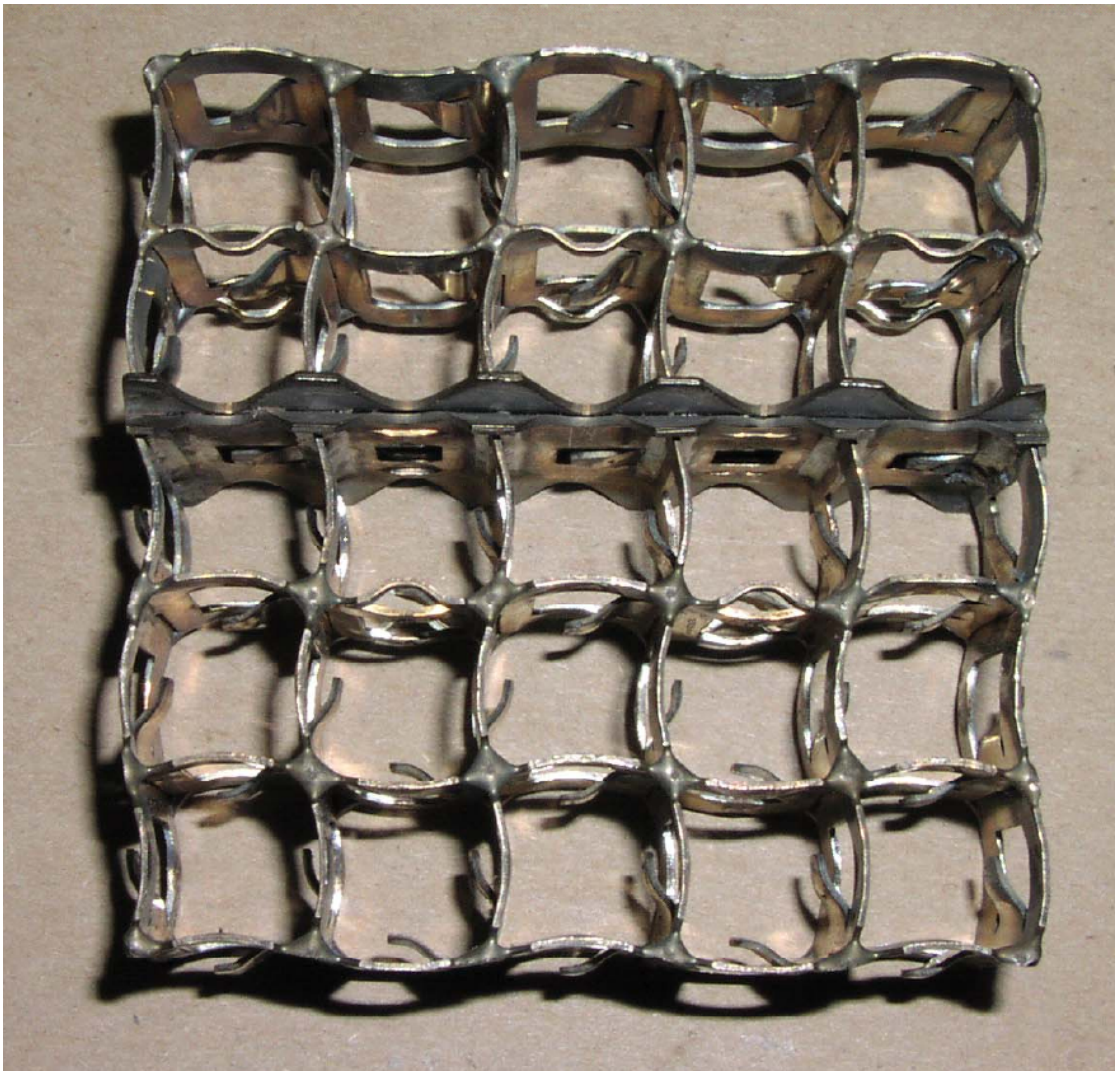

Figure 4.20: CE 5x5 Test 74 Mixing Vane Grid

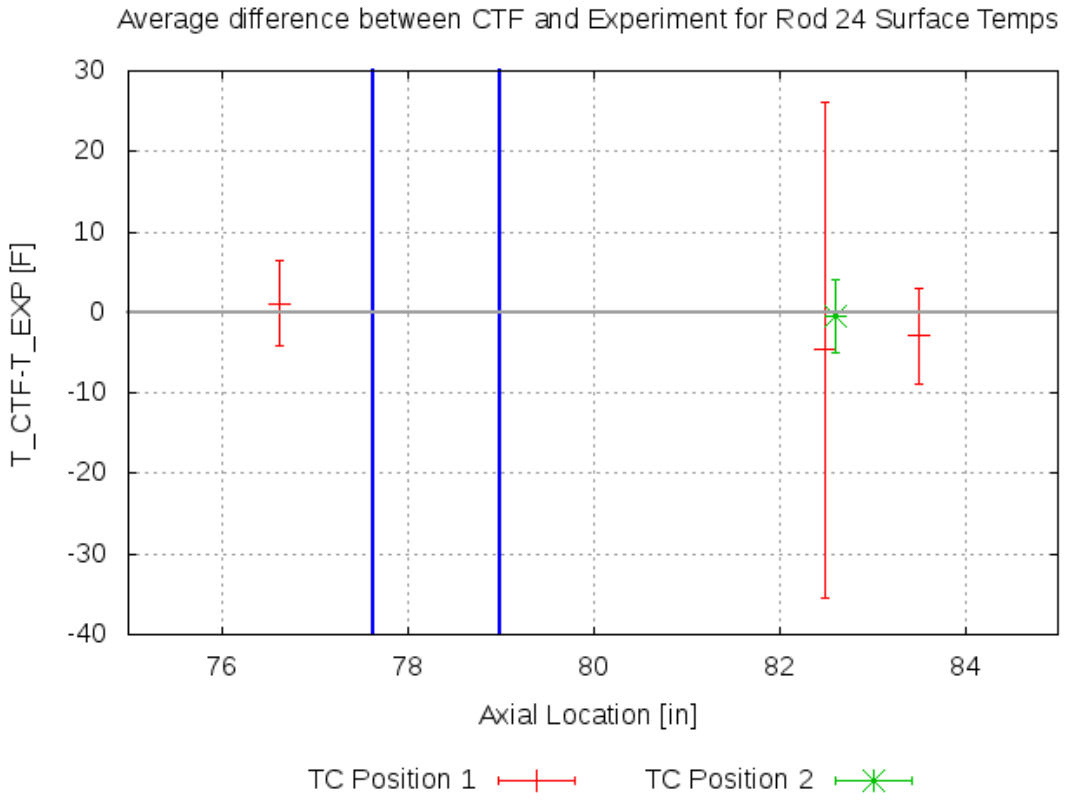

Figure 4.21: Summary of mean difference between predicted and measured rod surface temperatures for each thermocouple in Rod 24 over all test cases

4.7 Natural Circulation

Natural circulation does not classify as an "effect" like the previous sections; it is really a state of operation that has its own effects. However, because it may be of special interest to the user to see how CTF performs when modeling buoyancy-driven natural-circulation flows, it has been given its own section. The primary test of interest here is the PNNL 2x6 case, though the reader should be aware that the FRIGG facility, discussed in Sections 4.2.3 and 4.3.2 was also operated at natural circulation conditions.

4.7.1 PNNL 2x6 Tests

The facility was operated in two different scenarios; steady state and transient conditions. The steady-state results are discussed here. Two types of measurements were made in the facility: LDA local-velocity measurements and subchannel-center thermocouple measurements. Both of these measurement types were taken at five discrete axial locations in the bundle. The LDA measurements were taken along a single 1-D line, or "rake", in each of the three rows of subchannels. The thermocouple measurements were taken along a single 1-D rake in one of the rows of subchannels (the center row). The main difference between the two measurement types was that the LDA measurements were taken in finer increments, allowing for a mapping of the velocity profile within a subchannel, whereas the thermocouple measurements were only taken at subchannel centers.

The experimental results of these tests do not lend themselves as well to quantitative comparison with CTF predictions as well as for other effects that were discussed. This has to do with the fundamental differences between what the measurements and predictions mean. Concerning the velocity measurements, the values were local, so a velocity measurement taken at the center of the subchannel is much higher than that taken in the gap region between rods, where wall drag and viscous effects have a much larger impact on the fluid, leading to slower flows. While this appears in the measurements, the CTF prediction is one averaged velocity that includes these wall effects and smears them across the entire cross section of the subchannel.

One workaround to this problem is to average the LDA measurements, but this requires that the measurements be taken at equal intervals, so as not to weight some measurements more than others. This was not the case during the experiments. Additionally, the actual velocity values were not made available in the report but, rather, values were extracted from figures using a digitizer. A second option is to fit a correlation to each subchannel velocity profile and then integrate that curve over the bounds of the subchannel. Even this approach wouldn't be entirely accurate, however, as the subchannel dimensions where the LDA rake was made does not represent the geometry of the channel if we were to move the rake line closer or farther from us, the observer. In lieu of these considerations, the figures showing predicted and measured values are simply presented here for each window and rake location. The LDA results are presented in Figures 4.22 through 4.32.

In these figures, the LDA location in the rod bundle is shown on the x-axis. The y-axis of the figure shows a non-dimensionalized velocity at that measurement location (see Figure 3.6 for the meaning of the X and Y dimensions of the test assembly). Note in the results figures how the measured velocities will move above and below CTF values in many cases, which is expected, as

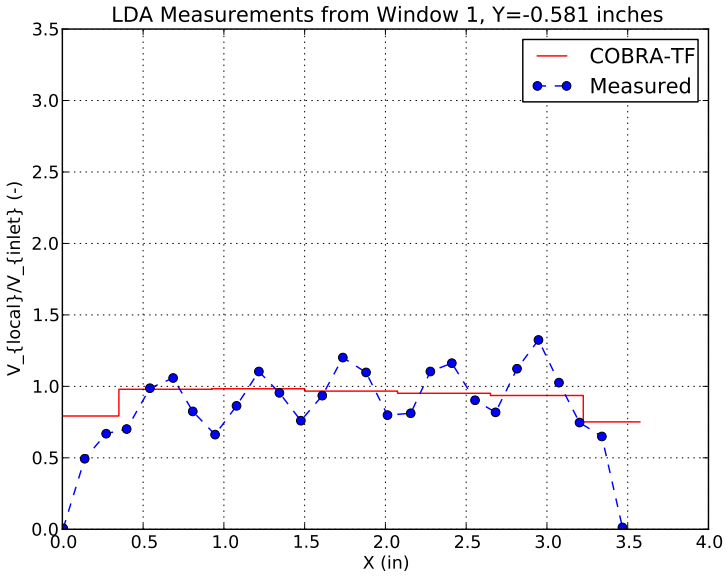

Figure 4.22: Predicted and measured subchannel velocities for Window 1 at Rake Location Y=-0.581 in in PNNL 2x6

the CTF values are a smeared, averaged value for the entire channel. The important thing to look for in these figures is that CTF is capturing the behavior of the velocity distribution, which should be for "left-side" velocities to be higher than "right-side" velocities due to the fact that only the "left-side" rods are heated. This uneven heating creates thermal plumes that drive the flow upwards on the left-side of the bundle.

CTF generally captures this behavior for all axial levels for rake locations at Y=0.0 inch and Y=0.581 inch. CTF tends to over-predict velocities for the Y=-0.581 inch rake location. However, the fact that measurements at rake location Y=-0.581 inch disagree with those at rake location Y=0.581 inch is a cause for concern because the measurements should agree due to symmetry of the test conditions. It was noted by the authors that there was a misalignment of the flow housing which accounts for this discrepancy. Since we do not capture this effect in CTF, we can disregard the disagreement of measured and predicted results for the Y=-0.581 inch rake location.

Figures 4.33 through 4.37 provide the comparison of measured and predicted temperature results for the 9 axial locations. These results will naturally suffer from the same problem as the velocity results. Here we are comparing a measurement of temperature taken at the center of the subchannel with a predicted value that is a smeared average over the whole subchannel. Being that most of these axial measurement locations are taken in a laminar flow, we expect very steep gradients in temperature as we move away from the wall. This accounts for the fact why we see an over-prediction of temperatures by CTF in many cases. However, note how this over-prediction only occurs in the lower axial regions of the bundle. When we move to the higher windows (7 and 9), the results match quite well. The reason for this is likely that the thermal plumes surrounding the rods have merged and led to a turbulent flow in the upper section of

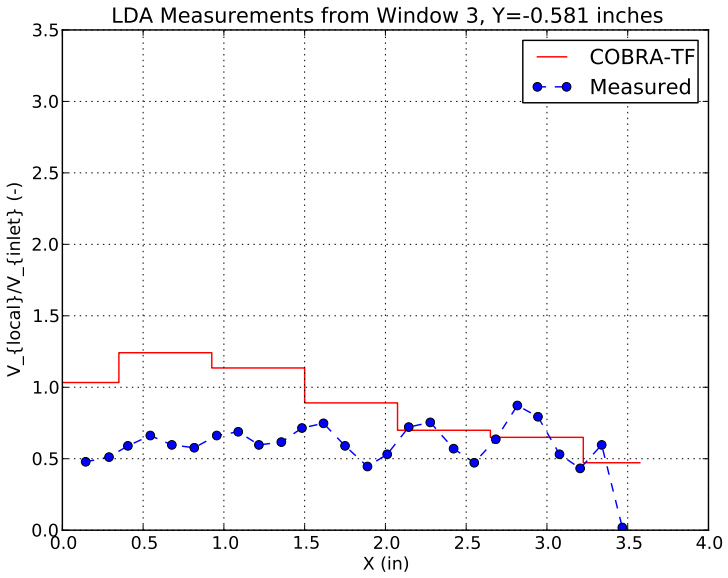

Figure 4.23: Predicted and measured subchannel velocities for Window 3 at Rake Location Y=-0.581 in in PNNL 2x6

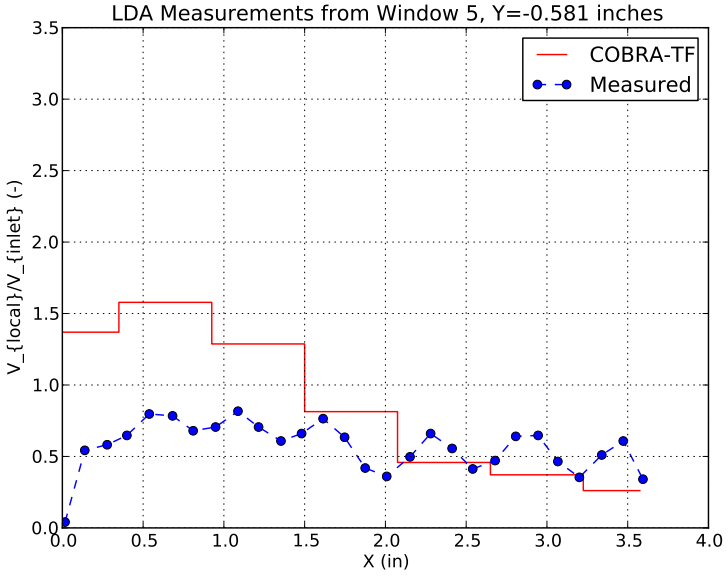

Figure 4.24: Predicted and measured subchannel velocities for Window 5 at Rake Location Y=-0.581 in in PNNL 2x6

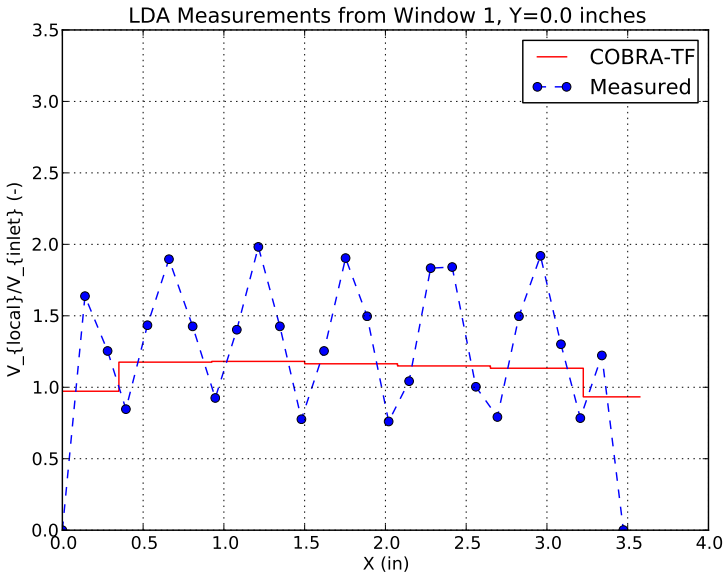

Figure 4.25: Predicted and measured subchannel velocities for Window 1 at Rake Location Y=0.0 in in PNNL 2x6

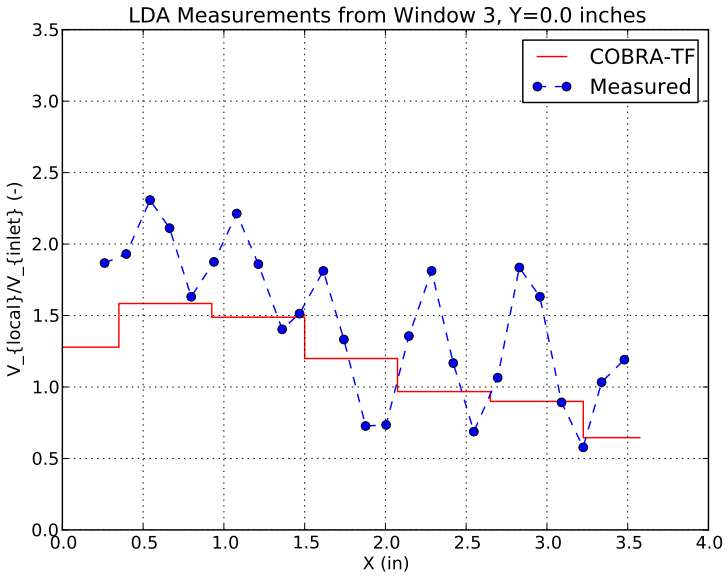

Figure 4.26: Predicted and measured subchannel velocities for Window 3 at Rake Location Y=0.0 in in PNNL 2x6

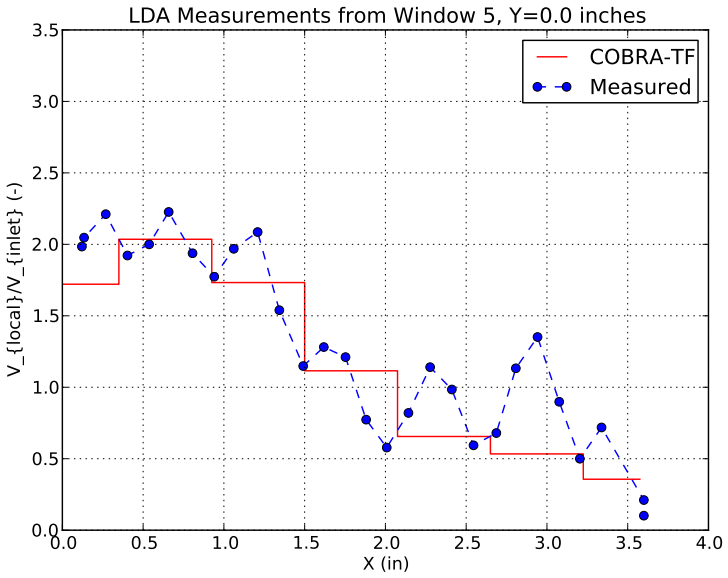

Figure 4.27: Predicted and measured subchannel velocities for Window 5 at Rake Location Y=0.0 in in PNNL 2x6

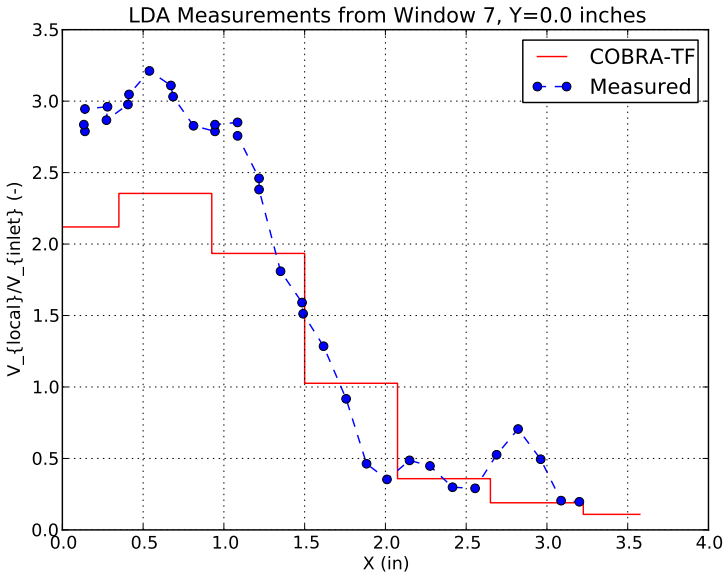

Figure 4.28: Predicted and measured subchannel velocities for Window 7 at Rake Location Y=0.0 in in PNNL 2x6

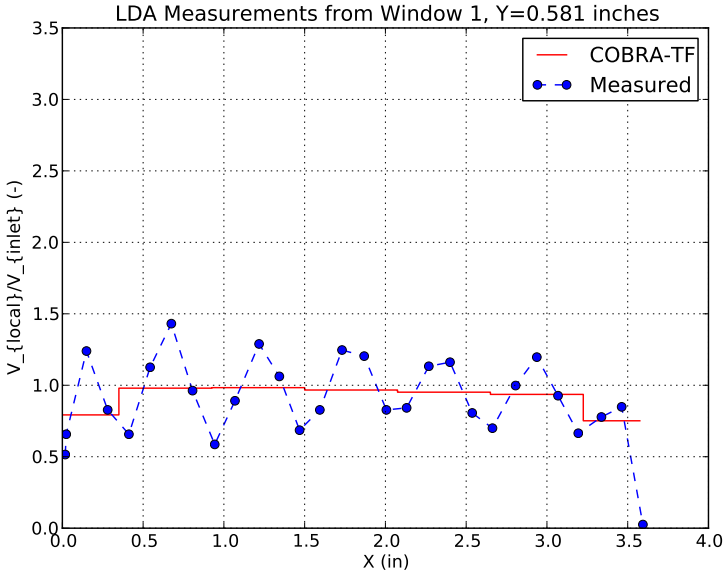

Figure 4.29: Predicted and measured subchannel velocities for Window 1 at Rake Location Y=0.581 in in PNNL 2x6

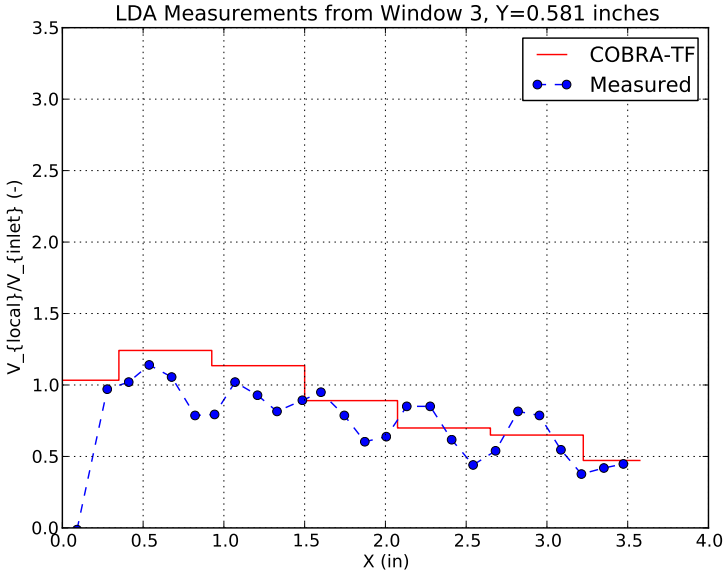

Figure 4.30: Predicted and measured subchannel velocities for Window 3 at Rake Location Y=0.581 in in PNNL 2x6

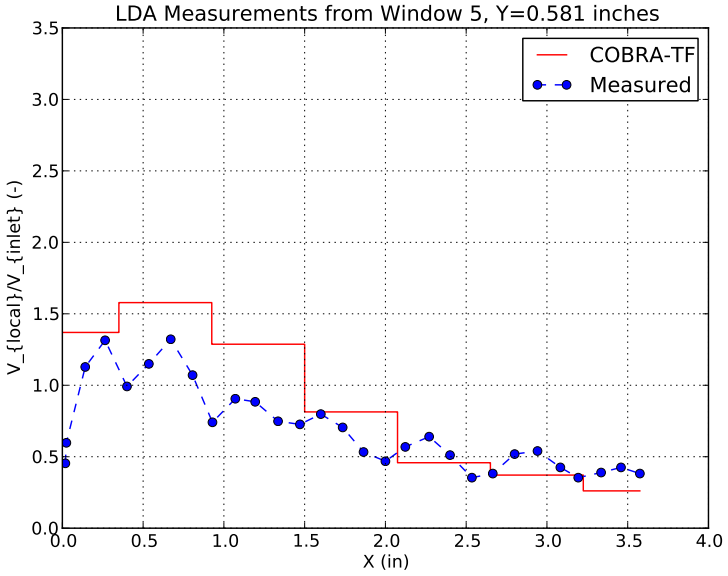

Figure 4.31: Predicted and measured subchannel velocities for Window 5 at Rake Location Y=0.581 in in PNNL 2x6

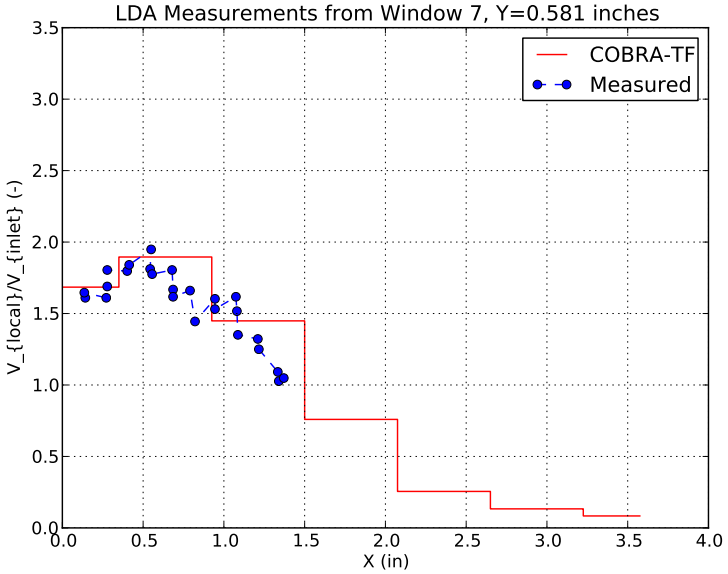

Figure 4.32: Predicted and measured subchannel velocities for Window 7 at Rake Location Y=0.581 in in PNNL 2x6

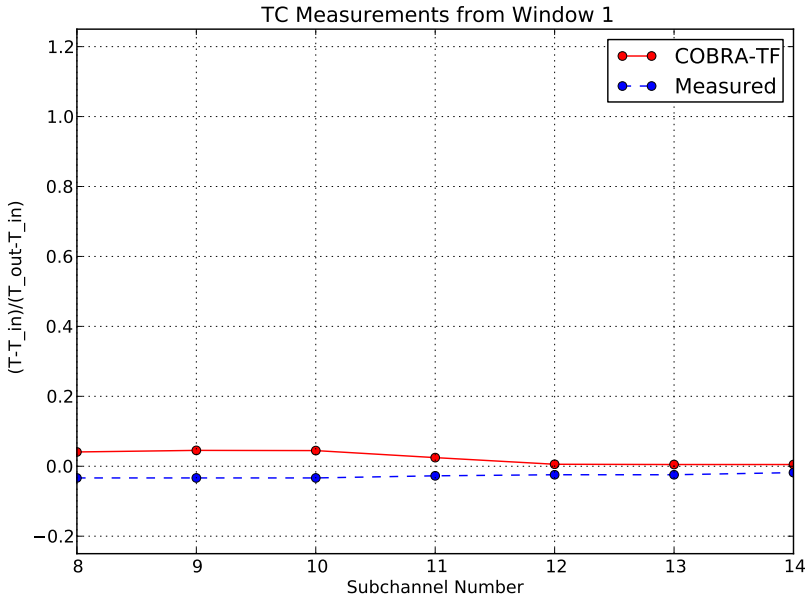

Figure 4.33: Predicted and measured subchannel-center temperatures for Window 1 in PNNL 2x6

the bundle. The increased turbulence acts to mix the fluid and reduce the temperature gradient across the subchannel. Data in this turbulent region will, naturally, match the volume-average results of CTF better.

Again, we need to concern ourselves with CTF's capability to match the behavior of the data. This is mostly the case except for the far-left side of the plots, where we see a drastic drop in measured temperatures. Since the entire left side of the bundle is heated, this drop in temperature is also unexpected. The predicted results are the behavior we would expect; temperatures should rise all the way up to the left side of the bundle. The authors noted this anomalous behavior, but did not provide a reason for its why it occurred.

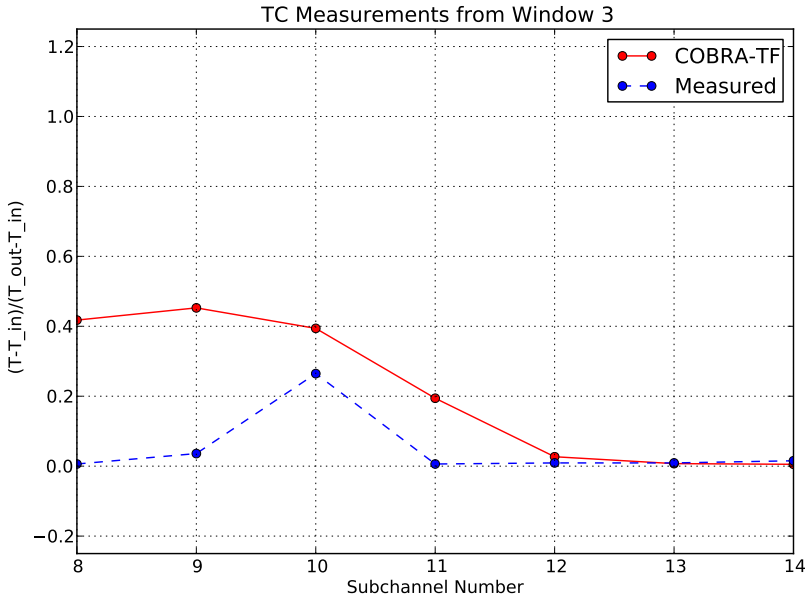

Figure 4.34: Predicted and measured subchannel-center temperatures for Window 3 in PNNL 2x6

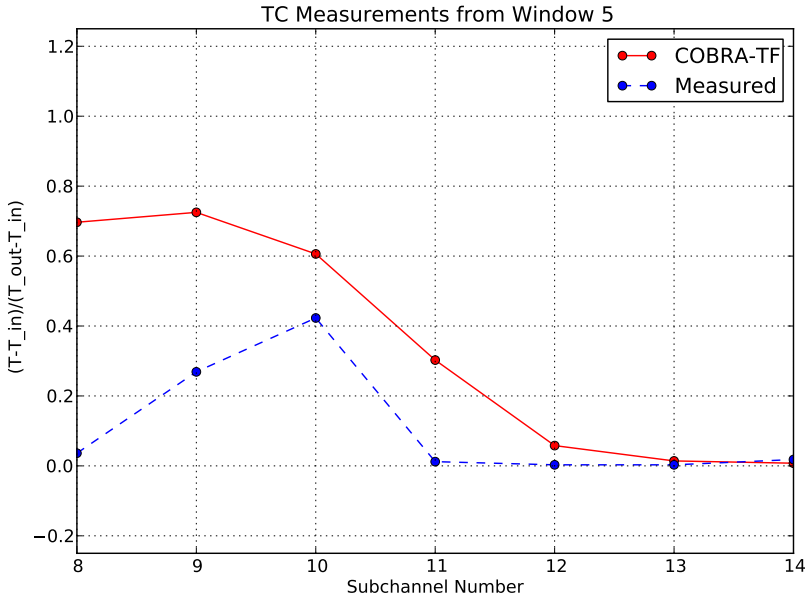

Figure 4.35: Predicted and measured subchannel-center temperatures for Window 5 in PNNL 2x6

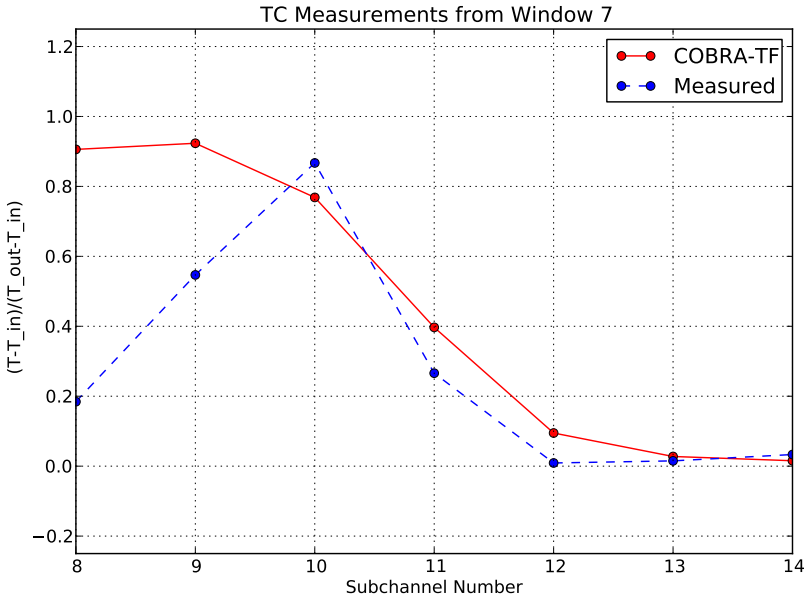

Figure 4.36: Predicted and measured subchannel-center temperatures for Window 7 in PNNL 2x6

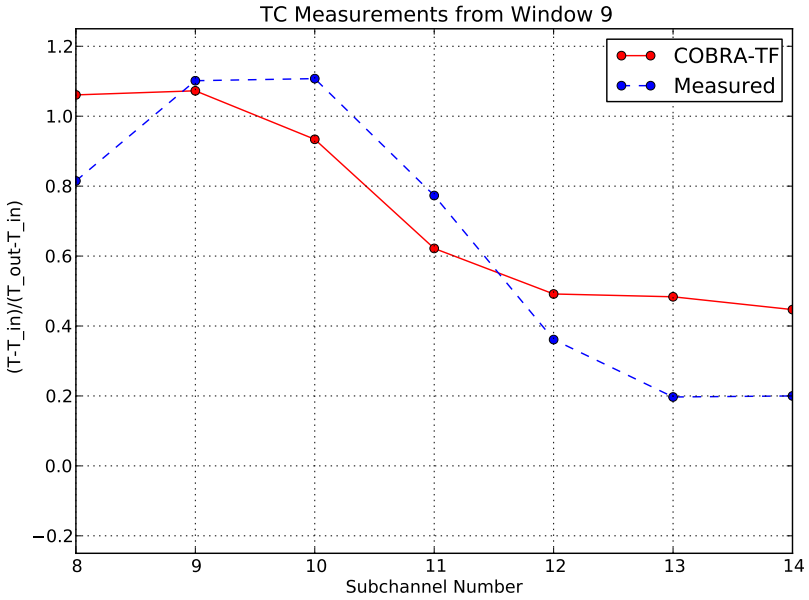

Figure 4.37: Predicted and measured subchannel-center temperatures for Window 9 in PNNL 2x6

CHAPTER 5

CONCLUSION

This document has been created as a key segment of the code testing approach for CTF. It outlines the code requirements (capabilities) and then demonstrates the code's ability to to meet a significant portion of those capabilities. A variety of tests have been chosen to target the most important features of CTF, including pressure drop, void, rod and coolant temperature, and mixing prediction in rod bundle geometries. Qualitative and quantitative analysis was performed to assess CTFs ability to capture the trends and behavior of phenomena as well as to present a general measure of its accuracy.

There are some noted shortfalls in the CTF testing and documentation matrix. Fist, the validation studies performed and included in this document are not an exhaustive measure of the CTF capabilities; there are still more CTF features, noted in Chapter 2, that have yet to be validated. Second, the experimental data employed to validate CTF does not specifically single out individual physical models in CTF; rather, they exercise several models in combination. An important part of code testing methodology is the QA measures used to ensure physics are coded up correctly and to keep bugs out of the source. While there are QA measures in place for CTF, this document only briefly touches on them. Much more thorough documentation is in line, describing the design of the many tests as well as their intention. Finally, more will need to be done and documented in the way of code verification and uncertainty quantification.

With these shortfalls noted, it is clear that there is more work to be done. However, this document does take great strides in improving CTF testing and validation. The tests modeled in this document act to exercise the most important code features of CTF. So long as the user is utilizing the code to model similar tests, utilizing the exercised features in this document, they can now have a greater confidence that CTF is actually capable of producing meaningful results. Furthermore, this document is meant to be a living document, giving the developers a forum for discussing future validation tasks and exercising different CTF capabilities.

BIBLIOGRAPHY

[1] M. Avramova H. Utsuno S. Bajorek A. Velazquez-Lozada A. Rubin, A. Schoedel. OECD/NRC BENCHMARK BASED ON NUPEC PWR SUBCHANNEL AND BUNDLE TESTS (PSBT). Technical report, US NRC and OECD Nuclear Energy Agency, 2010.

[2] L. Hochreiter K. Ivanov H. Utsuno F. Kasahara B. Neykov, F. Aydogan. NUPEC BWR Full-size Fine-mesh Bundle Test (BFBT) Benchmark. Technical report, NUCLEAR ENERGY AGENCY, 2006.

[3] J.M. Bates and E.U. Khan. Investigation of Combined Free and Forced Convection in a 2x6 Rod Bundle during Controlled Flow Transients. Technical Report PNL-3135, Battelle Pacific Northwest laboratories, 1980.

[4] A.W. Bennett, G.F. Hewlett, H.A. Kearsey, and R.K.F. Keeys. Heat transfer to steam-water mixtures flowing in uniformly heated tubes in which the critical heat flux has been exceeded. Technical Report AERE-R 5373, U.K.A.E.A. Research Group, Atomic Energy Research Establishement, 1967.

[5] Z. Karoutas, Y. Sung, Y. Chang, G. Kogan, and P. Joffre. Subcooled Boiling Data from Rod Bundles. Technical Report 1003383, EPRI, 2002.

[6] O. Nylund, K.M. Briker, R. Eklund, et al. FRIGG Loop Project. Technical Report R4-447/RTL-1007, AB Atomenergi, Stockholm, 1968.

[7] M.S. Quigley, C.A. McMonagle, and J.M. Bates. Investigation of Combined Free and Forced Convection in a 2x6 Rod Bundle. Technical Report BNWL-2216, Battelle Pacific Northwest Laboratories, 1997.

[8] D. W. Radcliffe R. T. Lahey Jr., B. S. Shirlakar. Two-Phase Flow and Heat Transfer In Multirod Geometries: Subchannel and Pressure Drop Measurements in a Nine-Rod Bundle for Diabatic and Adiabatic Conditions. Technical report, General Electric, 1970.

[9] R.K. Salko and M.N. Avramova. *CTF Theory Manual*. The Pennsylvania State University.

[10] B.S. Shiralkar and D.W. Radcliffe. An experimental and analytical study of the synthesis of grid spacer loss coefficients. Technical Report NEDE-13181, General Electric.

APPENDIX A

NOMENCLATURE

Acronyms

BFBT BWR Full-size Fine-mesh Bundle Tests

BOHL Beginning of Heated Length

BWR Boiling Water Reactor

CE Combustion Engineering

COBRA-TF Coolant-Boiling in Rod Arrays- Two Fluids

CTF PSU RDFMG version of COBRA-TF

CHF Critical Heat Flux

DNB Departure from Nucleate Boiling

GE General Electric

HTC Heat Transfer Coefficient

LDA Laser Doppler Anemometer

LWR Light Water Reactor

MV Mixing Vane

MVG Mixing Vane Grid

NMV Non-Mixing Vane

NUPEC Nuclear Power Engineering Corporation of Japan

PSBT PWR Sub-channel and Bundle Tests

PSU Pennsylvania State University

PWR Pressurized Water Reactor

QA Quality Assurance

QOI Quantity of Interest

RDFMG Reactor Dynamics and Fuel Management Group

rRMS relative root-mean-square

RMSE Root-mean-square error

T/H Thermal/Hydraulic

TPL Third-Party Library